Single-Crystal Spectral Studies of $Fe(SR)_4^-$ [R = 2,3,5,6-$(Me)_4C_6H$]: The Electronic Structure of the Ferric Tetrathiolate Active Site

Matthew S. Gebhard,[†] Joseph C. Deaton,[†] Stephen A. Koch,[‡] Michelle Millar,[‡] and Edward I. Solomon*,[†]

Contribution from the Department of Chemistry, Stanford University, Stanford, California 94305, and Department of Chemistry, SUNY Stony Brook, Stony Brook, New York 11794.
Received July 31, 1989

Abstract: Single-crystal polarized absorption, magnetic circular dichroism (MCD), and EPR spectroscopies have been employed to elucidate the electronic structure of the oxidized rubredoxin model complex $Fe(SR)_4^-$ [R = 2,3,5,6-$(Me)_4C_6H$]. These studies have led to a definitive assignment of the S_4 symmetry-split components of the $^6A_1 \rightarrow {}^4T_1{}^a$, $^4T_2{}^a$, and E^a spin-forbidden ligand field transitions, which are analyzed to give an experimental determination of the Fe d orbital axial splitting diagram. The transitions are correlated with the ground-state zero-field splitting (ZFS) to examine the origin of the large ZFS in ferric tetrathiolate complexes. As in our earlier studies[37] on a D_{2d} distorted T_d $Fe(Cl)_4^-$ complex, it is found that anisotropic covalency must be included to account for the observed ZFS. From comparisons to the data on D_{2d} $Fe(Cl)_4^-$ the orientation of the R group is found to determine the electronic structure of the iron tetrathiolate complex. A definitive assignment of the spin-allowed charge-transfer spectrum is presented. This is based on the polarized absorption data, and the sign and magnitude of the excited-state spin-orbit splittings as determined by single-crystal MCD spectroscopy. It is found that the charge-transfer spectrum is dominated by the thiolate S-pσ to Fe-dσ transitions (between 16 000 and 28 000 cm^{-1} with $\epsilon \approx$ 5000–10 000 M^{-1} cm^{-1}), with the S-pπ to Fe-dπ set of transitions at 13 000 cm^{-1} being weak ($\epsilon \approx 300$ M^{-1} cm^{-1}). This observation, along with the d orbital splitting pattern, and the lack of measurable in-state spin–orbit splitting of the $S_\pi \rightarrow Fe_\pi$ CT band indicate that the S_π bonding to the iron is not significant. In contrast, the dominance of the thiolate to iron σ bonding interaction is suggested by the d → d and CT data. This interaction is very dependent on the orientation of the thiolate R group. This thiolate S pσ bonding model is used to evaluate existing electronic structure calculations on ferric thiolates and is used to analyze the spectroscopic features of the oxidized rubredoxin active site.

The iron–sulfur proteins form an important class found throughout nature.[1] The most common structural types are the one-, two-, and four-iron–sulfur clusters, although the 3Fe–S clusters have received recent attention.[1d] Many of these proteins function in electron transport, but a variety of catalytic functions have been proposed.[1] The iron in these systems is approximately tetrahedral with all cysteinyl or mixed cysteinyl and sulfide ligation. The two- and four-iron clusters have two and four sulfides, respectively, with the sulfides bridging the iron atoms. Rubredoxin is the simplest iron–sulfur system, containing an approximately D_{2d} distorted $[Fe(S\text{-}Cys)_4]^-$ complex (Figure 1). The X-ray crystal structure[2] of *Clostridium pasteurianum* (*Cp*) rubredoxin has been solved to 1.2-Å resolution. Geometric and electronic structure/function relationships for rubredoxin and related model complexes have been investigated both experimentally[1-20] and theoretically.[21-24]

Rubredoxin exists in both ferric and ferrous oxidation states. The oxidized form of rubredoxin has some characteristic spectroscopic features. The EPR of all known rubredoxins[11] has a rhombic high-spin (HS) ferric EPR signal ($E/D \approx 0.25$) with $D > h\nu$ ($|D| \approx 1$–2 cm^{-1}). The sign of D has only been determined for *Pseudomonas oleovorans* rubredoxin[11] ($D = +1.68$ cm^{-1}); however, no crystal structure has been solved for this protein. It has been proposed that the large magnitude of this zero-field splitting (ZFS) is diagnostic of cysteinyl sulfur coordination. Although, more recently, large zero-field splittings have been found in HS ferric proteins[25] possessing no cysteinyl coordination. The absorption spectrum[1] of oxidized rubredoxin is dominated by a series of intense (ϵ = 5000–10 000 M^{-1} cm^{-1}) vis–UV charge-transfer transitions. None of the $^6A \rightarrow {}^4\Gamma$ spin-forbidden electronic transitions characteristic of a HS ferric complex have been definitively observed in the absorption or magnetic circular dichroism (MCD) spectra of rubredoxin, although this is expected because of the weak nature of these transitions. However, it has been suggested[26] that the characteristic 13 000-cm^{-1} absorption band (ϵ = 350 M^{-1} cm^{-1}) is the $^6A_1 \rightarrow {}^4T_1$ lowest energy spin-forbidden d → d transition. The magnetic Mössbauer spectrum[17] of oxidized rubredoxin shows an anomalously low nuclear hyperfine coupling.

[†] Stanford University.
[‡] SUNY Stony Brook.

(1) (a) *Iron Sulfur Proteins*; Lovenberg, W., Ed.; Academic Press: New York, 1973; Vols. I and II. (b) *Iron Sulfur Proteins*; Lovenberg, W., Ed.; Academic Press: New York, 1977; Vol. III. (c) *Metal Ions In Biology. Iron Sulfur Proteins*; Spiro, T. G., Ed.; Wiley-Interscience: New York, 1982; Vol. IV. (d) Kissinger, C. R.; Adman, E. T.; Sieker, L. C.; Jensen, L. H. *J. Am. Chem. Soc.* **1988**, *110*, 8721.
(2) (a) Watenpaugh, K. D.; Sieker, L. C.; Jensen, L. H. *J. Mol. Biol.* **1979**, *131*, 509. (b) Watenpaugh, K. D.; Sieker, L. C.; Jensen, L. H. *J. Mol. Biol.* **1980**, *138*, 615.
(3) Muraoka, T.; Nozawa, T.; Hatano, M. *Inorg. Chem. Acta* **1986**, *124*, 49.
(4) Rivoal, J. C.; Briat, B.; Cammock, R.; Hall, D. O.; Rao, K. K.; Douglass, I. N.; Thompson, A. J. *Biochim. Biophys. Acta* **1977**, *493*, 122.
(5) Eaton, W. A.; Palmer, G.; Fee, J. A.; Kimura, T.; Lovenberg, W. *Proc. Natl. Acad. Sci. U.S.A.* **1971**, *68*, 3015.
(6) Shulman, R. G.; Eisenberger, P.; Teo, B. K.; Kincaid, B. M.; Brown, G. S. *J. Mol. Biol.* **1978**, *124*, 305.
(7) Long, T. V.; Loehr, T. M. *J. Am. Chem. Soc.* **1970**, *92*, 6384.
(8) Long, T. V.; Loehr, T. M.; Allkins, J. R.; Lovenberg, W. *J. Am. Chem. Soc.* **1971**, *93*, 1809.
(9) Yachandra, V. K.; Hare, J.; Moura, I.; Spiro, T. G. *J. Am. Chem. Soc.* **1983**, *105*, 6455.
(10) Czernuszewicz, R. S.; LeGall, J.; Moura, I.; Spiro, T. G. *Inorg. Chem.* **1986**, *25*, 696.
(11) Peisach, J.; Blumberg, W. E.; Lode, E. T.; Coon, M. J. *J. Biol. Chem.* **1971**, *246*, 5877.
(12) Phillips, W. D.; Poe, M.; Weihler, J. F.; McDonald, C. C.; Lovenberg, W. *Nature (London)* **1970**, *227*, 574.
(13) Thompson, C. L.; Jackson, P. J.; Johnson, C. E. *Biochem. J.* **1972**, *129*, 1063.
(14) Eaton, W. A.; Lovenberg, W. In *Iron–Sulfur Proteins*; Academic Press: New York, 1973; Vol. II, pp 131–162.
(15) Eaton, W. A.; Lovenberg, W. *J. Am. Chem. Soc.* **1970**, *92*, 7195.
(16) Lane, R. W.; Ibers, J. A.; Frankel, R. B.; Papaefthymiou, G. C.; Holm, R. H. *J. Am. Chem. Soc.* **1977**, *99*, 84.
(17) Rao, K. K.; Evans, M. C. W.; Cammack, R.; Hall, D. O.; Thompson, C. L.; Jackson, P. J.; Johnson, C. E. *J. Biochem.* **1972**, *129*, 1063.
(18) Deaton, J. C.; Gebhard, M. G.; Koch, S. A.; Millar, M.; Solomon, E. I. *J. Am. Chem. Soc.* **1988**, *110*, 6241.
(19) Jacks, C. A.; Bennett, L. E.; Raymond, W. N.; Lovenberg, W. *Proc. Natl. Acad. Sci. U.S.A.* **1974**, *71*, 1118.
(20) Bennett, D. E.; Johnson, M. K. *Biochem. Biophys. Acta* **1987**, *911*, 71.
(21) Ueyama, N.; Sugawara, T.; Tatsumi, K.; Nakamura, A. *Inorg. Chem.* **1987**, *26*, 1978.

0002-7863/90/1512-2217$02.50/0

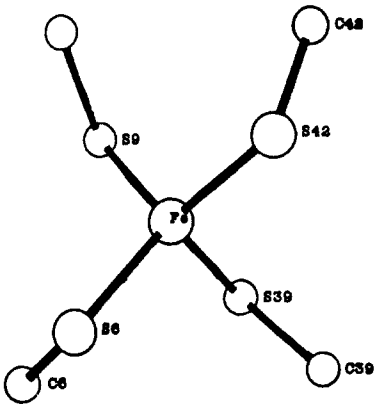

Figure 1. Active site of *Cp* rubredoxin as adapted from ref 2. View is down the pseudo-S_4 axis and shows sulfurs and α-carbons.

This has been attributed to a high degree of covalency in the site and appears to be diagnostic of sulfur coordination.[27]

It is believed that the function of rubredoxin is to mediate electron transfer.[1] The reduction potential[1] of these proteins is roughly −0.06 V relative to a standard hydrogen electrode, which is much lower than the aqueous ferric/ferrous couple (+0.77 V). While, part of this low reduction potential can be attributed to the coordination of four negatively charged residues, there appears to be an intrinsic stabilization of the ferric relative to the ferrous ion, due to coordination by thiolates. It is also clear[1] that the protein environment raises the reduction potential, as most ferric/ferrous tetrathiolate model complexes have reduction potentials at roughly −1 V versus SHE. An intriguing feature of rubredoxin is its very fast electron-transfer self-exchange rate of roughly 10^9/s. A thorough understanding of the electronic structure factors that contribute to these redox properties is important for elucidating how rubredoxin and the more complex multinuclear Fe–S centers function.

In this work single-crystal polarized absorption, MCD, and EPR have been employed to define the electronic structure of a ferric rubredoxin model complex[28-30] $[[Fe(SR)_4][N(C_2H_5)_4]$, where R = 2,3,5,6-$(CH_3)_4C_6H$]. This complex is well suited for detailed spectroscopy, due to the strict S_4 site symmetry (Figure 2), the uniaxial $I\bar{4}$ space group, and the overall quality and size of the single crystals. While $(S(CH_3)_4C_6H)^-$ is not strictly a biologically relevant ligand, it is similar enough to alkyl thiolates to allow comparisons to the protein site.

The single-crystal polarized spectrum of the spin-forbidden d→d transitions and the EPR results on the $Fe(SR)_4$ model complex have been reported in a preliminary communication.[18] The ligand field spectral region is now described in detail and extended to include the entire charge-transfer spectral region. These data are analyzed by using selection rules based on vector coupling coefficients, which allow a rigorous assignment of the spectrum. Based on these data, a bonding model is developed that accounts for the structural characteristics that influence the electronic structure of ferric tetrathiolate complexes. Spectroscopic correlations between oxidized rubredoxin and the model complex are also presented, thus yielding an assignment of the charge-transfer spectrum of oxidized rubredoxin and providing an experimental measure of the bonding interaction in this protein active site.

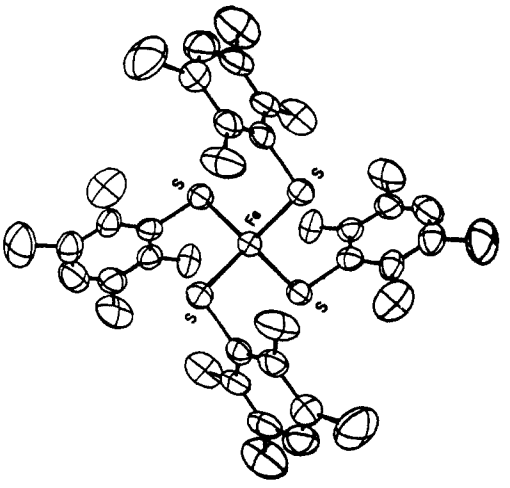

Figure 2. Structure of the $[Fe(SR)_4]^-$ [R = 2,3,5,6-$(Me)_4C_6H$] anion viewed down the S_4 axis.

Experimental Section

$[Et_4N][Fe(SR)_4]$ [R = 2,3,5,6-$(CH_3)_4C_6H$] was prepared by mixing ethanol solutions of LiSR and anhydrous $FeCl_3$ with a 5:1 mole ratio. The solution was stirred for approximately 10 min, and the complex was precipitated as the Et_4N^+ salt. The reaction was run under N_2 using deoxygenated solvents. Single crystals[29] of $[Et_4N][Fe(SR)_4]$ were grown by dissolving the complex in hot dry DMF. The solution was filtered and allowed to cool slowly over several days. The compound crystallizes in the $I\bar{4}$ space group with the crystals displaying the full symmetry of the space group. The crystals grow as flattened tetrahedra (1–2 mm on edge) in the {101} closed form. The iron atom occupies a site of rigorous S_4 site symmetry,[29] with the molecular S_4 axis (z axis) coinciding with the crystal c axis. The FeS_4 core is slightly distorted from tetrahedral symmetry with a compression along the S_4 axis causing the S–Fe–S angles bisected by the S_4 axis to open to 114.4°. The other four angles are 102.4°. The Fe–S bond length is 2.284 ± 0.002 Å. The gallium(III) analogue is isomorphous[29] to the Fe(III) salt and is used as a host lattice for experiments requiring dilute concentrations of the ferric complex. The gallium salt was prepared with $GaCl_3$ by the above procedure. Doped crystals were grown as with the pure crystals after mixing desired amounts of the Ga and Fe compounds. The actual Fe concentration tended to be smaller than the nominal concentration due to decomposition of the ferric complex in solution. The crystal concentration was determined by measuring the absorption at 775 nm (ϵ = 304 M^{-1} cm^{-1}) or at 588 nm (ϵ = 5600 M^{-1} cm^{-1}).

For single-crystal EPR experiments, doped crystals (1% Fe) were mounted with grease to the end of a quartz rod that fit snugly in an EPR tube. The rod was cut to complement the interfacial angle between the (101) and ($\bar{1}$01) faces of the crystal. This allowed the crystal to be oriented with the c axis either parallel or perpendicular to the magnetic field. A powder pattern EPR spectrum was obtained on doped crystals (0.5% Fe).

For optical experiments, the (101) face was mounted flush against a quartz window, secured with an optically transparent resin (Crystalbond), and masked off around the edges with black electrical tape. Crystals were polished to the desired thickness with 9 μm grit lapping film or a homemade polishing apparatus. The polarized absorption spectrum was recorded with the E vector polarized parallel or perpendicular to the projection of the c axis on the (101) face. When the E vector is perpendicular to the c axis, the spectrum is purely x,y polarized. The parallel orientation yields a mixed polarization spectrum (36% x,y + 64% z). The z-polarized spectrum was determined by subtracting 36% of the pure x,y polarization from the mixed polarization and renormalizing. Single-crystal MCD spectra were recorded on crystals that were cut and polished on the (001) face and prepared in the same manner as for the optical experiments. In this orientation light is propagated down the crystal c axis, such that the E vector has no projection on the molecular z axis. In addition, MCD spectra were recorded on a mull of the pure compound, which was pulverized and suspended in thoroughly degassed mineral oil. The mull was spread between quartz windows. Depolarization of the light by the MCD samples was monitored by the effect the sample had on the CD signal of nickel (+)-tartrate placed before and after the sample. Samples that decreased the CD signal by less than 5% were considered suitable.

(22) Bair, R. A.; Goddard, W. A., III *J. Am. Chem. Soc.* **1978**, *100*, 5669.
(23) Noodleman, L.; Norman, J. G., Jr.; Osborne, J. H.; Aizman, A.; Case, D. A. *J. Am. Chem. Soc.* **1985**, *107*, 3418.
(24) Norman, J. G., Jr.; Jackels, S. C. *J. Am. Chem. Soc.* **1975**, *97*, 3833.
(25) Que, L., Jr.: Lipscomb, J. D.; Zimmermann, R.; Munck, E.; Orme-Johnson, N. R.; Orme-Johnson, W. H. *Biochim. Biophys. Acta* **1976**, *452*, 320.
(26) Rawlings, J.; Siiman, O.; Gray, H. B. *Proc. Natl. Acad. Sci. U.S.A.* **1974**, *71*, 125.
(27) Que, L., Jr. Non-Heme Iron Deoxygenases. *Struct. Bonding (Berlin)* **1980**, *40*, 39.
(28) Koch, S. A.; Maelia, L. E.; Millar, M. *J. Am. Chem. Soc.* **1983**, *105*, 5944.
(29) Millar, M.; Lee, J. F.; Koch, S. A.; Fikar, R. *Inorg. Chem.* **1982**, *21*, 4105.
(30) Maelia, L. E.; Koch, S. A. *Inorg. Chem.* **1986**, *25*, 1896.

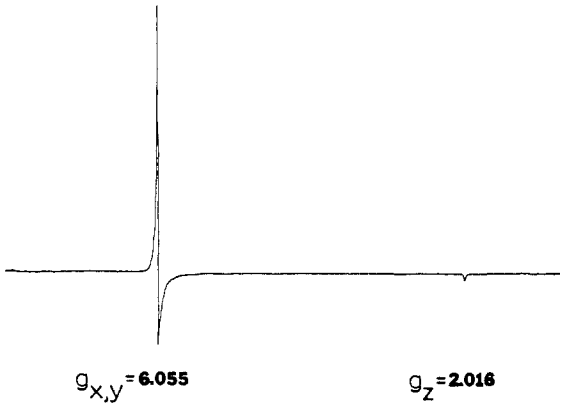

Figure 3. Powder pattern EPR spectrum of $[NEt_4][Ga\{Fe\}(SR)_4]$ ([Fe] = 1%) at 10 K, 9.390 GHz, 1 mW, and 2 G modulation.

Polarized absorption spectra were measured on a McPherson RS-10 double-beam spectrophotometer described previously,[31] but with upgraded electronics. A pair of Glan-Taylor polarizers matched from 200 nm to 2.5 μm were used to polarize the sample and reference beams. Three gratings blazed at 3000 Å, 7500 Å, and 1.25 μm were used to cover the different spectral regions. An extended S-20 photomultiplier tube covered the region from 2200 to 8000 Å and a dry ice cooled S-1 tube covered from 5000 Å to 1 μm. A Joule-Thompson cooled PbS detector was used from 8500 Å to 2.5 μm. The latter detector required use of a chopped (560 Hz) light source and a lock-in amplifier. The light sources were a tungsten–halogen lamp for the visible and near-IR regions and a deuterium lamp for the near-UV. Variable-temperature absorption experiments from 300 to 2 K were done with a Janis Super-Vari Temp Dewar. MCD spectra were recorded on a Jasco J-500C CD spectropolarimeter configured with an Oxford SM4 superconducting magnet and focusing optics, described previously.[32] EPR spectra were recorded on a Bruker ER 220D spectrometer with X-band (9.4 GHz) or Q-band (34 GHz) microwave bridge systems. For the X-band experiments, temperatures from 4.2 to 300 K were achieved with an Air Products LTR3 liquid helium refrigerator, while for Q-band experiments, temperatures down to 100 K were achieved with a Bruker flow system using cold nitrogen gas. Precise magnetic field determinations were made with a Bruker ER035M NMR Gaussmeter, while the microwave frequency was calibrated with a Hewlett-Packard HP5342A microwave frequency counter. The precise orientation of the axial crystal relative to the magnetic field was determined by observation of the turning points in the angular dependence of the EPR resonance.

Results

(a) Ground-State Electron Paramagnetic Resonance. The X-band (9.4-GHz) powder pattern EPR spectrum of 0.5% Fe in $[Et_4N][Ga(Fe)(SR)_4]$ is presented in Figure 3. The approximate $g_z = 2$ and $g_{x,y} = 6$ pattern for the $-^1/_2 \rightarrow +^1/_2$ transition with no other transitions observed up to 14 kG is indicative[33] of an axial HS ferric site with $|D| \gg h\nu$ ($h\nu = 0.31$ cm^{-1}). The axial pattern is expected because the Fe occupies a site of strict S_4 symmetry.

The axial zero-field splitting (ZFS) parameter, D, was determined by two independent methods. The temperature dependence[34] of the integrated EPR signal for the $-^1/_2 \rightarrow +^1/_2$ transition for a single crystal of $[Et_4N][Ga(Fe)(SR)_4]$ gave $D = +2.5 \pm 0.5$ cm^{-1}. This method has the advantage of giving the sign of D. The second method employed the equations derived by Kirkpatrick,[35] which relate differences in the effective $g_{x,y}$ for the $-^1/_2 \rightarrow +^1/_2$ transition measured at different magnetic fields. Kirkpatrick has shown that the effective $g_{x,y}$ for the for the $-^1/_2 \rightarrow +^1/_2$ transition is slightly perturbed by an off-diagonal Zeeman interaction with the $M_s = \pm^3/_2$ level. If $|D| \gg h\nu$, this interaction can be treated by third-order perturbation theory to solve for $|D|$ and the true $g_{x,y}$. Using Kirkpatrick's expressions, and the effective $g_{x,y}$ values (6.055 ± 0.005 at 1.1143 ± 0.0001 kG and 5.981 ± 0.003 at 4.0793 ± 0.0002 kG), gives $|D| = 2.4 \pm 0.1$ cm^{-1} and $g_{x,y} = 2.021 \pm 0.002$. While this method gives a more accurate measure of $|D|$, it does not give the sign of D; however, from the temperature dependence described above, D is positive. In addition, $g_z = 2.0159 \pm 0.0007$. It should be noted that both g values show a deviation from the free electron value of 2.0023, indicating that spin–orbit coupling between the ^6A ground state and $^6\Gamma$ charge-transfer states must contribute.[36-38] Lastly, because of the large value of D, the fourth power zero-field splitting terms (a and F) can be neglected.

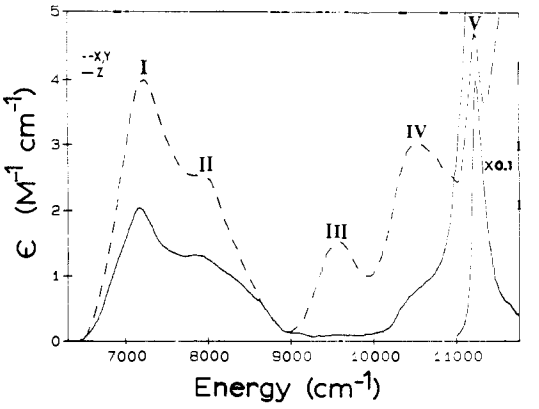

Figure 4. Polarized absorption spectrum (101 face) of 0.7 mm thick $[NEt_4][Fe(SR)_4]$ at 2 K.

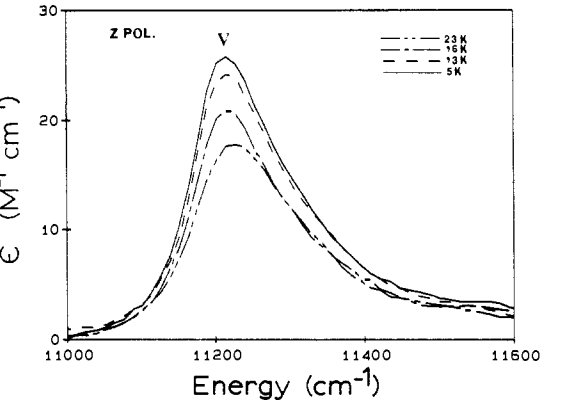

Figure 5. Variable-temperature z-polarized absorption spectrum (101 face) of 0.1 mm thick $[NEt_4][Fe(SR)_4]$.

(b) Ligand Field Excited States. (i) Polarized Absorption. The polarized absorption spectrum on a pure single crystal of $[Et_4N][Fe(SR)_4]$ in the region from 6250 to 11 750 cm^{-1} is presented in Figure 4. Electronic absorption bands were distinguished from vibrational absorption in the near-IR by comparison of the absorption spectrum of the pure Fe crystal with the pure Ga analogue. The spectrum reveals five excited electronic states (labeled I–V) in this region with molar extinction coefficients below 10 M^{-1} cm^{-1}. The low intensity is characteristic[37] of spin-forbidden ligand field transitions in HS tetrahedral ferric complexes. These states are the only detectable electronic absorption transitions between 12 000 and 4000 cm^{-1}.

Bands I (7250 cm^{-1}) and II (7975 cm^{-1}) exhibit mixed polarizations although both are more intense in the x,y polarization ($x,y/z \approx 2$). Bands III (9540 cm^{-1}) and IV (10 525 cm^{-1}) are dominantly x,y polarized. Band V (11 255 cm^{-1}) shows the rather intriguing behavior (vida infra) of being mostly z polarized ($z/x,y \approx 9$). The x,y polarization of band V is approximately the same magnitude as the other ligand field states while the z polarization is 9 times more intense.

(31) Wilson, R. B.; Solomon, E. I. *Inorg. Chem.* **1978**, *17*, 1729.
(32) Allendorf, M. D.; Spira, D. J.; Solomon, E. I. *Proc. Natl. Acad. Sci. U.S.A.* **1985**, *82*, 3063.
(33) Blumberg, W. E.; Piesach, J. *Ann. N.Y. Acad. Sci.* **1973**, *222*, 529.
(34) Que, L., Jr.; Lipscomb, J. D.; Munck, E.; Wood, J. M. *Biochim. Biophys. Acta* **1974**, *485*, 60.
(35) Kirkpatrick, E. S.; Muller, K. A.; Rubins, R. S. *Phys. Rev.* **1964**, *135A*, 86.
(36) (a) Watanabe, H.; Kishishita, H. *Prog. Theor. Phys.* **1970**, *46*, 1. (b) Watanahbe, H. *J. Phys. Chem. Solids* **1964**, *25*, 1471. (c) Watanabe, H. *Progr. Theor. Phys.* **1957**, *18*, 405.
(37) Deaton, J. C.; Gebhard, M. G.; Solomon, E. I. *Inorg. Chem.* **1989**, *28*, 877.
(38) MoriGaki, K.; Hoshina, T. *J. Phys. Soc. Jpn.* **1966**, *21*, 842.

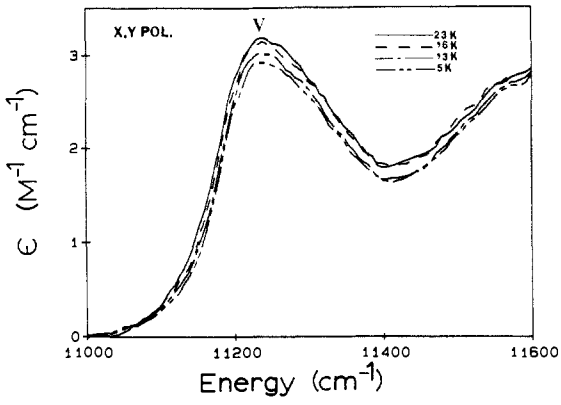

Figure 6. Variable-temperature x,y-polarized absorption spectrum (101 face) of 0.9 mm thick $[NEt_4][Fe(SR)_4]$.

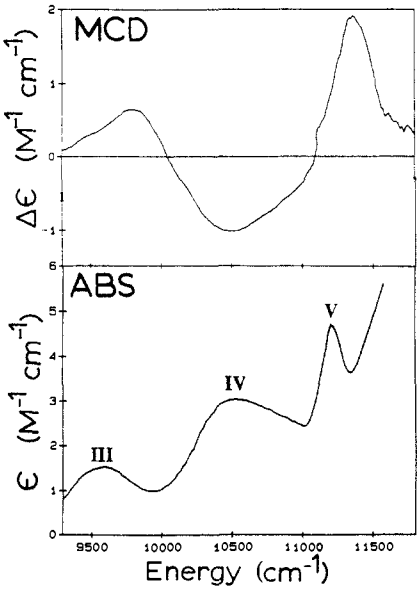

Figure 7. Single-crystal MCD spectrum (001 face) of 0.28 mm thick $[NEt_4][Fe(SR)_4]$ at 2 K and 60 kG (top), shown along with x,y-polarized absorption spectrum (bottom).

An additional temperature-dependent effect was observed for the z polarization of band V (Figure 5). As the temperature of the sample was lowered from 30 to 5 K the integrated intensity of the z-polarized absorption band increased by 40%, while the x,y-polarized intensity (Figure 6) showed very little change and in fact decreased slightly as the temperature was lowered. All states to higher energy of band V show no intensity change between 50 and 5 K.

(ii) Magnetic Circular Dichroism. The low-temperature MCD spectrum on a pure single crystal of $[Et_4N][Fe(SR)_4]$ for the region of bands III–V is shown in Figure 7 along with the x,y-polarized absorption spectrum, since for an oriented uniaxial single crystal it is necessary but not sufficient for a band to have x,y-polarized intensity in order to have nonzero MCD intensity. Because an S-1 photomultiplier tube was used for the MCD experiments, bands below 9400 cm^{-1} could not be recorded. This low-energy cutoff is also responsible for the asymmetry observed in the MCD band shape of band III. Bands III–V all exhibited temperature-dependent c-term behavior, which is expected[39] for spin-forbidden ligand field transitions in HS ferric complexes. Band III gives a positive C term ($C_0/D_0 \approx 2$), band IV a negative C term ($C_0/D_0 \approx -2$), and band V a positive C term ($C_0/D_0 \approx 1$).

(c) Charge-Transfer States. (i) Polarized Absorption. Figure 8 shows the polarized absorption spectrum for the first observed transition to higher energy of band V. The band (A) is dominantly

(39) Stephens, P. J. *Adv. Chem. Phys.* **1976**, *35*, 197.

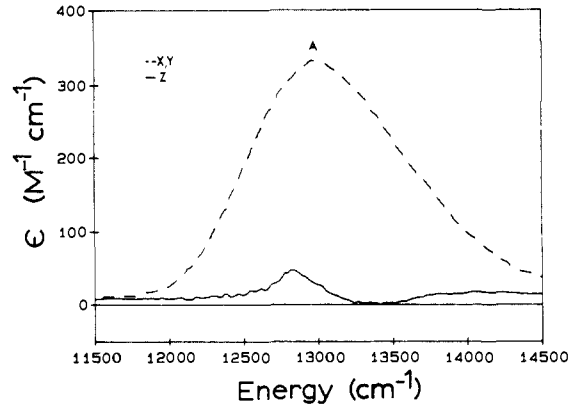

Figure 8. Polarized absorption spectrum (101 face) of 0.1 mm thick $[NEt_4][Ga\{Fe\}(SR)_4]$ ([Fe] = 10%) at 10 K.

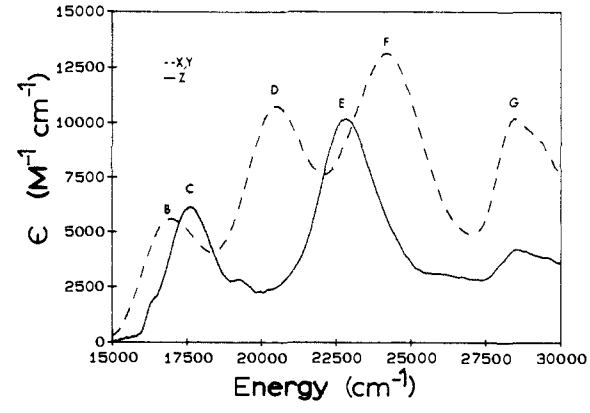

Figure 9. Polarized absorption spectrum (101 face) of 0.05 mm thick $[NEt_4][Ga\{Fe\}(SR)_4]$ ([Fe] = 1%) at 6 K.

x,y polarized and has an intensity that can be correlated with the Fe(III) concentration. The intensity of this transition (340 M^{-1} cm^{-1}) is intermediate between what is typically observed[37] for a fully allowed charge-transfer transition and a spin-forbidden transition. For reasons to be elucidated in the Analysis section this transition is spin-allowed and therefore must be the lowest energy charge-transfer state.

Figure 9 shows the polarized absorption spectra from 14 500 to 32 000 cm^{-1}. All transitions observed in this region have intensities that correlate with the Fe(III) concentration. Transitions above 32 000 cm^{-1} are independent of Fe(III) concentration and must be intraligand or counterion in origin. On the basis of their intensities ($\epsilon > 4000$ M^{-1} cm^{-1}) the absorption bands between 14 500 and 32 000 cm^{-1} are fully dipole-allowed transitions and, with the exception of band G (vide infra), are assigned as the ligand to metal charge-transfer transitions. The bands are labeled B–G. Bands C (17 800 cm^{-1}) and E (22 300 cm^{-1}) are strongly z polarized. Bands B (17 000 cm^{-1}), D (20 440 cm^{-1}), and F(24 800 cm^{-1}) are strongly x,y polarized. Band G (29 000 cm^{-1}) shows mixed polarizations, $I_{x,y}/I_z \approx 3.5$.

(ii) Magnetic Circular Dichroism. The single-crystal MCD spectrum from 12 000 to 32 000 cm^{-1} of $[Et_4N][Ga(SR)_4]$ doped with 0.5% Fe(III) is presented in Figures 10 and 11 along with the corresponding x,y-polarized absorption spectrum. All of the MCD signals up to 27 500 cm^{-1} exhibited temperature-dependent C-term behavior.[39]

The MCD spectrum reveals a positive C term centered at 13 100 cm^{-1} (Figure 10) in the energy region of band A in the x,y-polarized absorption spectrum. This band is labeled M_1, because the orientationally averaged mull MCD spectrum (vida infra) indicates that this MCD feature must arise from a different electronic state than band A.

The MCD spectrum of the higher energy charge-transfer transitions is more complex due to overlapping bands. To facilitate the analysis, the MCD signal was fit by using a nonlinear curve fitting routine.[40] Two types of band-shape functions were em-

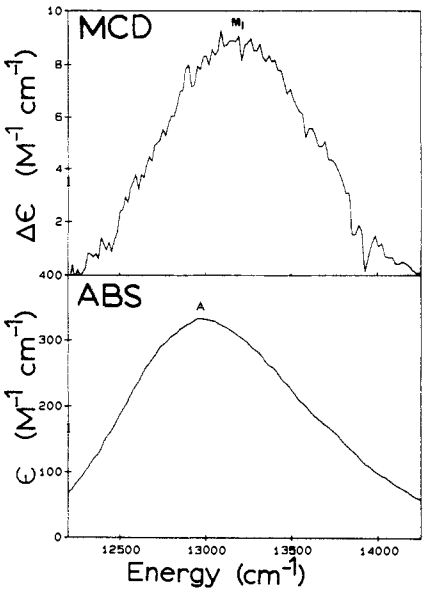

Figure 10. Single-crystal MCD spectrum (001 face) of 0.1 mm thick $[NEt_4][Ga\{Fe\}(SR)_4]$ ([Fe] = 0.2%) at 80 K and 60 kG (top), shown along with x,y-polarized absorption spectrum (bottom).

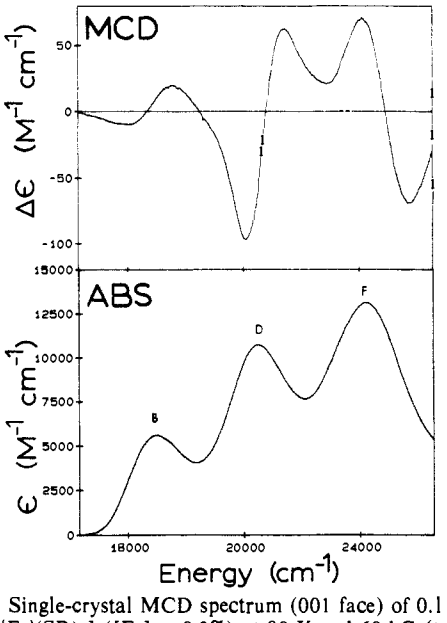

Figure 11. Single-crystal MCD spectrum (001 face) of 0.1 mm thick $[NEt_4][Ga\{Fe\}(SR)_4]$ ([Fe] = 0.2%) at 80 K and 60 kG (top), shown along with x,y-polarized absorption spectrum (bottom).

ployed. *C* terms were modeled with a Gaussian function defined by three parameters (energy, bandwidth, and peak height). Pseudo-*A* terms were modeled with a band shape derived from two overlapping Gaussians of opposite sign at different energies and are defined by four parameters (average energy, bandwidth, peak height, and energy splitting between the Gaussians). The experimental MCD spectrum was fit in the region from 14 300 to 26 500 cm^{-1}. The best fit with the least number of bands and most reasonable parameters requires contributions from three pseudo-*A* terms and four additional *C* terms. The resolved MCD features along with the total band-shape and experimental data are shown in Figure 12. The energies for each of the bands are given in Table I. Each of the three pseudo-*A* terms is centered about an absorption peak in the x,y-polarized spectrum (bands B, D, and F in Figure 9). The two positive MCD *C* terms have peaks at the same energy as the two z-polarized absorption bands (bands C and E in Figure 9). The two negative *C* terms (M_3 and

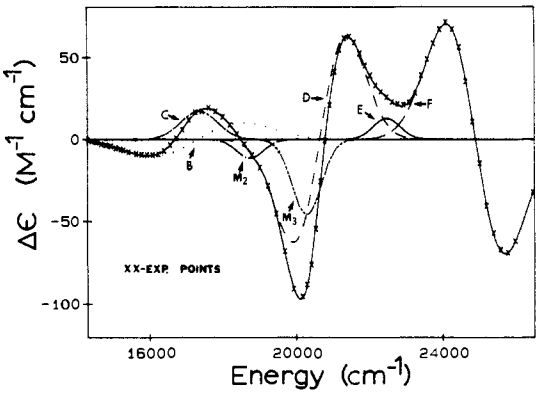

Figure 12. Resolved fit of the single-crystal MCD spectrum (Figure 11) showing three *A* terms (B, D, and F) and four *C* terms (C, M_2, M_3, and E), along with the total band shape and experimental data points (only $^1/_3$ shown for clarity).

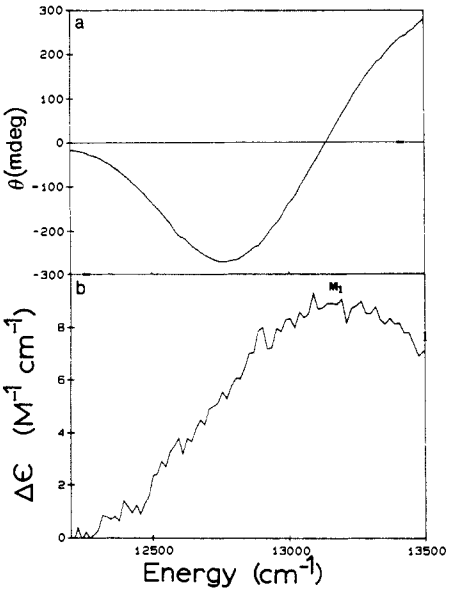

Figure 13. (a) Mull MCD spectrum at 5 K and 60 kG. (b) Single-crystal MCD spectrum (001 face) at 80 K and 60 kG.

Table I

band	energy, cm^{-1}	0th moment, 10^3 cm^{-1}	1st moment,[b] 10^3 cm^{-1}	λ, cm^{-1}	ζ, cm^{-1}
B	17 000	1860[a]	25 ± 6	300 ± 100	150 ± 50
C	17 500	3.8[b]			
M_3	18 700	−1.7[b]			
M_4	20 300	−6.7[b]			
D	20 650	1450[a]	87 ± 20	590 ± 150	295 ± 75
E	22 450	1.6[b]			
F	24 900	750[a]	−97 ± 30	−500 ± 125	−250 ± 60
G	29 000	500[a]			

[a] Calculated from absorption band. [b] Calculated from single-crystal MCD.

M_4) do not appear to be associated with any of the observed electronic absorption bands.

By use of the band shapes calculated for the pseudo-*A* terms, the splitting of the two-component *C* terms giving rise to the pseudo-*A* term was determined. This is accomplished from a moment analysis[41] of the MCD signal and the corresponding polarized absorption band. The moment of an absorption or MCD band is defined in the standard manner (eq 1). α is the intensity

$$\langle \alpha/E \rangle_n = \int \alpha(E)[(E - E_0)^n/E]\, dE \qquad (1)$$

(40) Johnson, K. J. *Numerical Methods in Chemistry*; Marcel Dekker: New York, 1980.

(41) Piepho, S. B.; Schatz, P. N. *Group Theory in Spectroscopy*; Wiley-Interscience: New York, 1983.

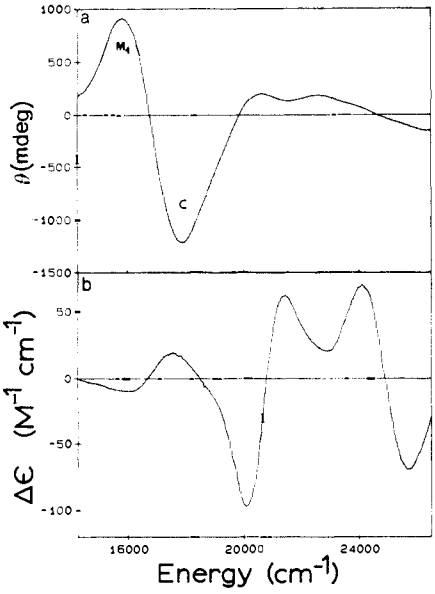

Figure 14. (a) Mull MCD spectrum at 5 K and 60 kG. (b) Single-crystal MCD spectrum (001 face) at 80 K and 60 kG.

of the polarized absorption or MCD signal, and n is the moment about the energy, E_0, which is chosen so that the first moment of a Gaussian-shaped absorption band is zero (i.e., the energy of the crossing point of the A term). The results are summarized in Table I.

Additional MCD data were obtained on a mull of the pure compound (Figure 13 and 14). The mull MCD spectrum was recorded to 36 500 cm^{-1} and none of the MCD signals above 27 000 cm^{-1} showed any temperature dependence. A striking feature of the mull spectrum is its difference from the single-crystal MCD spectrum (Figures 10 and 11). The 13 100-cm^{-1} single-crystal MCD feature (band M_1) changes sign in the mull MCD spectrum. Additionally, two MCD features not prominent in the single-crystal MCD spectrum are dominant in the mull spectrum in the region from 15 000 to 19 000 cm^{-1} (Figure 14). The positive signal (band M_2) at 15 800 cm^{-1} is new; however, the negative peak at 17 550 cm^{-1} corresponds to the observed z-polarized absorption band (C) and positive single-crystal MCD feature at 17 500 cm^{-1}.

Analysis

(a) Ligand Field Transitions. (i) Selection Rules for Polarized Absorption. It is evident from the highly polarized nature of the ligand field transitions in the $Fe(SR)_4^-$ complex (Figure 4) that the effective site symmetry is less than tetrahedral even though the FeS_4 core of the molecule is only slightly distorted from tetrahedral structure. Thus the analysis must be done using the S_4 axial subgroup. Although the effective site symmetry is less than tetrahedral, the cubic point group is a useful starting point for a discussion of the electronic structure of this complex.

In tetrahedral symmetry, a HS Fe(III) complex will have the following quartet excited states in order of increasing energy:[42] $^4T_1{}^a$, $^4T_2{}^a$, $^4A_1$, and $^4E^a$. The S_4 axial distortion splits the $^4T_1{}^a$ and $^4T_2{}^a$ states into the tetragonal basis states $^4T_1{}^a(z)$, $^4T_1{}^a(x,y)$ and $^4T_2{}^a(z)$, $^4T_2{}^a(x,y)$. The $^4T_1{}^a(x,y)$ and $^4T_2{}^a(x,y)$ transform as E states and are allowed to mix. This mixing could be large in the present case but will not change the group theoretically determined selection rules. To first order the distortion will not split the θ and ϵ orbital components of the $^4E^a$ state because it derives from the $t_2{}^3e^2$ strong-field configuration and is therefore ligand field independent.[43] However, the degeneracy of the $^4E^a$ orbital components can be lifted through a configuration interaction with the z orbital component of a $^4T_2$ state because both the $^4E(\epsilon)$ orbital component and the $^4T_2(z)$ component have B symmetry in S_4. This effect could be significant because the $^4T_2{}^b$ and $^4E^a$ states can be close in energy, as was observed in the HS ferric tetrachloride complex[37] (within 600 cm^{-1}).

Table II

^4h	θ	I_z	$I_{x,y}$	$I_z(\pm^5/_2)$	$I_{x,y}(\pm^5/_2)$	C_0/D_0	$(C_0/D_0)_{tot}$
$^4T_1$	z	0	1		1.5	−7	−7/2
	x,y	2	1	1.5	0	0	
$^4T_2$	z	0	1		1.5	+7	+7/2
	x,y	2	1	1.5	0	0	
^4E	θ	0	3		1.5	−7	−7/2
	ϵ	4	1	0	1.5	+7	

Because the point group S_4 is an invariant subgroup of D_{2d}, selection rules derived in D_{2d} will carry over to the corresponding states in S_4, as long as there is only limited mixing between states or orbitals that transformed as B_1 and B_2 or A_1 and A_2 in D_{2d}. The selection rules for the spin-forbidden transitions in the D_{2d} HS iron site in $[AsPh_4][FeCl_4]$ have been derived.[37] In D_{2d} symmetry the z components of the orbital triplet states ($^4T_1$ or $^4T_2$) will be purely x,y polarized, and the x,y components of both orbital triplet states will exhibit mixed polarizations. The θ component of a ^4E will be purely x,y polarized, while the ϵ component will have a z:x,y polarization ratio of 4:1. This information is summarized in the third and fourth column of Table II. In T_d symmetry the integrated intensity for a given band must be the same in x,y or z polarizations. As the symmetry is lowered to S_4 the components of the band will no longer be degenerate, but as long as the wave functions remain unchanged on lowering the symmetry from T_d to S_4, the integrated intensity in z polarization will equal the integrated intensity in the x,y polarization when summed over all the low-symmetry-split components of the T_d state. From Figure 4 it is evident this is not the case for $Fe(SR)_4^-$, indicating that there has been a change in the wavefunctions. A similar effect was observed[37] in the ferric tetrachloride polarized absorption spectrum and is attributed to covalency differences among the Fe(III) d orbitals.

On the basis of their mixed polarizations, the states at 7250 (band I) and 7975 cm^{-1} (band II) can be assigned as x,y components of the $^4T_1{}^a$ or $^4T_2{}^a$ states, while the purely x,y-polarized states at 9540 (band III) and 10 528 cm^{-1} (band IV) can be assigned as z components of the $^4T_1{}^a$ or $^4T_2{}^a$ states. The state at 11 240 cm^{-1} (band V) does not show the characteristic polarization behavior of any of the spin-forbidden transitions; however, on the basis of the relatively narrow bandwidth of the peak, it should be a ligand field independent state (i.e., the $^4E^a$ or second $^4T_2{}^b$ state). Energy ordering considerations[42] support the $^4E^a$ assignment; however, this alone is not sufficient to rule out the $^4T_2{}^b$ state.

(ii) Magnetic Circular Dichroism. An analysis[37] of the MCD results (Figure 7) on bands III and IV allows a definitive assignment of these two states. From Table II, column 7, the z component of the $^4T_1{}^a$ state gives rise to a negative MCD C term ($C_0/D_0 = -7$) while the z component of the $^4T_2{}^a$ state gives a positive C term ($C_0/D_0 = 7$). Thus band III is the z component of the $^4T_2{}^a$ state, while band IV is the z component of the $^4T_1{}^a$ state. Therefore, band I (Figure 4) must be the x,y component of the $^4T_1{}^a$ state and band II the x,y component of the $^4T_2{}^a$ state. A reverse order of I and II would place the barycenter of the $^4T_2{}^a$ state energetically below the $^4T_1{}^a$ state, which is not reasonable based on the theory of Tanabe and Sugano[42] for a d^5 ion in a cubic crystal field.

Band V (Figure 7), which can be either the $^4E^a$ or $^4T_2{}^b$ state, appears to be associated with a positive MCD C term. In T_d symmetry, the positive MCD feature is only consistent with the $^4T_2{}^b$ state, while the $^4E^a$ state is required to have a negative MCD C_0/D_0 ratio. However, the $^4E^a$ state is predicted[42] to be energetically below the $^4T_2{}^b$ state, and there are no bands to lower energy of band V that are candidates for the $^4E^a$ state. An alternative explanation for the sign of the MCD is possible. From Table II, the θ and ϵ components of the $^4E^a$ state have C terms of opposite sign with the θ component being negative and the ϵ component positive. In a tetrahedral molecule the x,y-polarized intensity of the θ component is 3 times larger than the ϵ component; thus, the θ dominates and the MCD is negative. If the ϵ intensity

(42) Tanabe, Y.; Sugano, S. *J. Phys. Soc. Jpn.* **1954**, *9*, 753.
(43) Goode, D. H. *J. Chem. Phys.* **1965**, *43*, 2830.

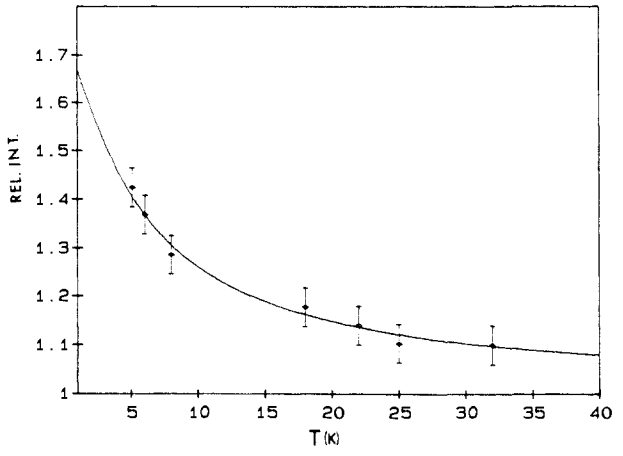

Figure 15. Theoretical temperature dependence (solid line) of z-polarized absorption spectrum of a ^{4}E state along with the experimental data points.

become enhanced relative to the θ when the symmetry is lowered to S_4, then the MCD for the ^{4}E^a state can change sign. A similar effect must occur for the ^{4}T$_1{}^a$ and ^{4}T$_2{}^a$ states as the polarization ratios show a major deviation from the predicted tetrahedral values. It is also possible that the ^{4}E^a θ component is to higher energy of band V and is buried under the more intense absorption band at 12900 cm^{-1} (band A).

(iii) Temperature Dependence of Polarized Absorption Intensity. In the study[37] of [AsPh$_4$][FeCl$_4$] it was found that spin-forbidden transitions in HS ferric complexes have absorption intensities that depend on the ground spin state M_s value. The expression for the intensity of a given transition from any one of the ground spin states is given in eq 6a,b of ref 37. The intensity-gaining mechanism derived for the D_{2d} FeCl$_4^-$ complex predicts (Table II, columns 5 and 6) that x,y-polarized intensity [$I_{x,y}(-^5/_2)$] from the $M_s = \pm 5/2$ spin level will be zero if the excited state is an x,y orbital component of a ^{4}T$_1$ or ^{4}T$_2$, and the z-polarized intensity from the $M_s = \pm^5/_2$ sublevel [$I_z(-^5/_2)$] will be zero if the excited state is the ϵ orbital component of a ^{4}E. If the population of the ground-state doublets can be perturbed so that only the $M_s = \pm^5/_2$ spin level is populated, then the transition intensity will go to zero for the above states. This effect was observed[37] in the transverse Zeeman effect on the D_{2d} FeCl$_4^-$ complex, by placing the FeCl$_4^-$ complex in 5-T magnetic field at 2 K to selectively populate the $M_s = -^5/_2$ substate. In these experiments on the FeCl$_4^-$ complex, it was observed that the x,y components of the ^{4}T$_1{}^a$ and ^{4}T$_2{}^a$ states lost all their x,y-polarized absorption intensity. A similar effect was observed for z polarization of the ^{4}E^b state[37] in the FeCl$_4^-$ complex.

In the absence of a magnetic field the spin-forbidden transitions will still display a temperature-dependent absorption intensity if the populations over the ZFS split M_s sublevel can be perturbed. In the Fe(SR)$_4$ complex, $D = +2.4$ cm^{-1}. The $M_s = \pm^1/_2$ doublet is the ground state with the $M_s = \pm^3/_2$ and $M_s = \pm^5/_2$ at 4.8 and 14.4 cm^{-1}, respectively. Qualitatively, the relative intensity will increase as the temperature is lowered if the transition has no intensity from the $M_s = \pm^5/_2$ doublet.

In Figure 5 the z polarization of band V shows a definite increase as the temperature is decreased (i.e., decreasing population of the $\pm^5/_2$ sublevel). As seen in Table II, this is only consistent with assignment of the z polarization of band V as the ϵ component of the ^{4}E state. Further, the relative temperature dependence of the z polarization of band V quantitatively fits the ^{4}E^a theoretical temperature dependence (Figure 15), which is given by eq 2. In

$$I(T) = [^6/_5 + (^9/_5)\exp(-2D/kT)]/[1 + \exp(-2D/kT) + \exp(-6D/kT)] \quad (2)$$

eq 2, D is the ZFS (2.4 cm^{-1}). Equation 2 was derived by using the relative intensities for transitions from the different sublevels ($M_s = \pm^1/_2, \pm^3/_2$, and $\pm^5/_2$, where $I = {}^6/_5, {}^9/_5$, and 0, respectively) weighted by their Boltzmann population at a given temperature.

Table III

band	energy, cm^{-1}	pol abs ($z/x,y$)	MCD (C_0/D_0)	assgnmt
I	7250	mixed (0.5)		^{4}T$_1(x,y)$
II	7975	mixed (0.5)		^{4}T$_2(x,y)$
III	9540	x,y	+2	^{4}T$_2(z)$
IV	10525	x,y	−2	^{4}T$_1(z)$
V	11225	mixed (9)	+1	^{4}E(ϵ)

The calculated transition intensity was normalized to the intensity when all three sublevels are equally populated. The experimentally determined intensities were normalized to the intensity at T = 32 K. As a control it was determined that all the transitions (bands A–H) to higher energy of band V had intensities that were independent of temperature between 5 and 50 K.

The temperature-dependent z-polarized absorption intensity of band V requires that the z-polarized transition is the ϵ orbital component of the ^{4}E^a state. The positive single-crystal MCD signal associated with band V indicates that the x,y polarization also arises from the ϵ orbital component of the ^{4}E^a state. The highly z-polarized nature of this transition ($z/x,y \approx 9$) is also consistent with this assignment, because in tetrahedral symmetry the ^{4}E$^a\epsilon$ component has a $z/x,y = 4$.

(iv) Ligand Field Analysis. By use of the observed and assigned d → d transitions (Table III) a ligand field analysis has been performed to extract the one-electron Fe(III) d orbital splitting pattern and to estimate the electron repulsion parameters (B and C). Employing the full Tanabe–Sugano[42] matrices for d^5 ligand field states gives a best fit with the ligand field parameters: C = 2222 cm^{-1}, B = 22 cm^{-1}, and Dq = −480 cm^{-1}. The electron repulsion parameter B is drastically reduced from the free ion value, indicating that an extreme covalent interaction is present in this complex. If the electron repulsion parameters are reexpressed as the Condon–Shortley integrals, the results are F_2 = 340 cm^{-1} and F_4 = 63 cm^{-1}. A comparison with the free ion values[44] (F_2 = 1666 cm^{-1} and F_4 = 111.9 cm^{-1}) reveals that F_2 is much more reduced than F_4, a result that is supported by theoretical calculations,[45] which predict that F_2 is more sensitive to outer orbital properties than F_4. This reduction is so large that the electron repulsion parameters obtained from the ligand field analysis cannot be considered reliable. The splitting between the ^{4}E^a and ^{4}T$_1{}^a$ or ^{4}T$_2{}^a$ states is sensitive to the value of Dq but is relatively insensitive to the electron repulsion parameters. Thus, while the absolute energies of the ^{4}E^a, ^{4}T$_1{}^a$, and ^{4}T$_2{}^a$ states will depend on the values of B and C, the splitting between the ^{4}E^a and ^{4}T$_1{}^a$ or ^{4}T$_2{}^a$ states will depend mostly on Dq, as long as the reduction in electron repulsion from the free ion values is similar for all three states. Because the value of Dq is not strongly coupled to the electron repulsion parameters for these three states, the Dq determined from fitting the energies of these states to the Tanabe–Sugano matrices is more reliable.

The S_4 ligand field one-electron orbital splitting pattern of the t$_2$ and e tetrahedral antibonding sets was determined from an analysis of the ^{4}T$_2{}^a$ and ^{4}T$_1{}^a$ axial field splittings. The low-symmetry splittings of the many-electron states in the strong-field limit can be expressed in terms of the splittings of the constituent one-electron orbitals[43] and is given by eq 3. δ is the energy

$$\Delta^4T_1(t_2{}^4e^1) = -\Delta^4T_1(t_2{}^2e^3) = \delta + (^3/_4)\mu \quad (3a)$$

$$\Delta^4T_2(t_2{}^4e^1) = -\Delta^4T_2(t_2{}^2e^3) = \delta - (^3/_4)\mu \quad (3b)$$

$$\Delta^4T_2(t_2{}^3e^2) = \Delta^4T_2(t_2{}^3e^2) = 0 \quad (3c)$$

separation between the Fe$_\sigma$-e($d_{xz,yz}$) and Fe$_\sigma$-b(d_{xy}) orbitals and is positive if the doubly degenerate set is at higher energy. μ is the separation between the Fe-b($d_{x^2-y^2}$) and Fe$_\pi$-a(d_{z^2}) orbitals and is defined to be positive if Fe$_\pi$-a(d_{z^2}) is at lower energy. The low-symmetry splitting, Δ^4T_i, is defined to be positive if the doubly degenerate component is at higher energy. If mixing between strong-field configurations is neglected,[46] then μ = 2700 cm^{-1} and

(44) Reader, J.; Sugar, J. *J. Phys. Chem. Ref. Data* **1975**, *4*, 397.
(45) Ferguson, J. *Prog. Inorg. Chem.* **1970**, *12*, 195.

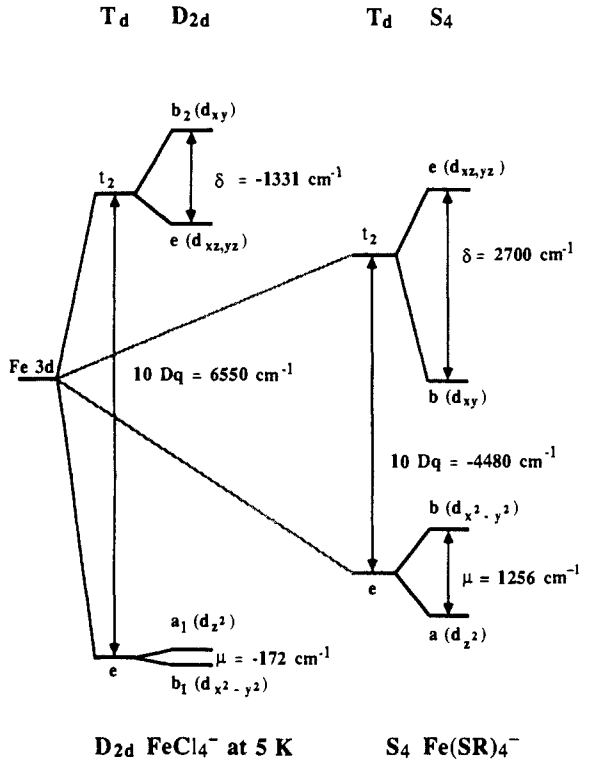

Figure 16. Experimentally determined Fe d orbital splitting pattern for D_{2d} $FeCl_4^-$ [37] and S_4 $[Fe(SR)_4]^-$.

δ = 1200 cm^{-1}. This means that the Fe_σ-e($d_{xz,yz}$) orbitals have a stronger antibonding interaction with the thiolate ligands than does the Fe_σ-b(d_{xy}) orbital. This experimental quantitative d orbital splitting pattern is summarized in Figure 16, along with the experimental order observed[37] for D_{2d} $FeCl_4^-$.

(b) Charge-Transfer Transitions. (i) Polarized Absorption. It is first necessary to define the set of ligand valence orbitals, which are primarily thiolate sulfur 3p in character. The sulfur–carbon σ bond is the dominant sulfur 3p bonding interaction. The interaction[47] of a S 3p orbital with the α-C will cause this S 3p orbital (S–C_σ) to be at low energy relative to the Fe 3d orbitals and directed toward the α-C and away from the Fe 3d orbitals. The large energy difference and poor overlap of this S–C_σ orbital relative to the Fe 3d orbitals precludes a strong bonding interaction with the metal center. In the free thiolate ligand, the other two S 3p orbitals are perpendicular to the S–C bond. The S 3p orbital, which is perpendicular to the phenyl ring, is stabilized through conjugation with the π system. Based on the geometry[29] of the ferric tetrathiolate complex (Figure 2), this S 3p orbital is pointed almost along the Fe–S bond and is mostly σ bonding with the metal 3d orbitals (Figure 17a). The Fe–S–C_α bond angle of 102.4° rotates this orbital off the Fe–S bond. The third S 3p orbital is perpendicular to the other two and is in the plane of the ring. This orbital is perpendicular to the Fe–S bond, lies in the S–Fe–S plane containing the molecular S_4 axis, and is purely π bonding with the metal 3d orbitals (Figure 17b). Thus, two S 3p orbitals on each ligand have significant bonding interactions with the Fe 3d orbitals. These form the sets of mostly σ bonding and purely π bonding symmetry-adapted linear combinations (SALCs) given in Table IV. The irreducible representations in S_4 for both the σ and π bonding SALCs are a, b, and e (S_4 in Figure 18). While the S_π-b ligand SALC has the correct symmetry to interact with the Fe_π-b($d_{x^2-y^2}$) orbital, these orbitals have poor overlap. In addition, the S_π-e is of correct symmetry to interact with the mostly σ antibonding Fe_σ-e($d_{xz,yz}$) orbitals, but these also have poor overlap.

(46) It was found for the D_{2d} $FeCl_4^-$ complex that inclusion of the second and third strong-field configurations changed the parameters δ and μ by less than 5%.

(47) Gewirth, A. A. Ph.D. Thesis, Stanford University, 1987.

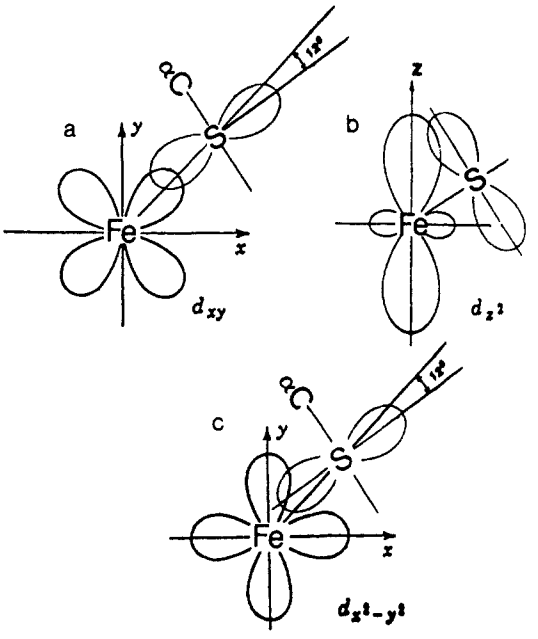

Figure 17. (a) Decreased overlap between the Fe-(d_{xy}) orbital and one of the off-axis S_σ orbitals, viewed down S_4 axis. (b) Overlap between the Fe-(d_{z^2}) orbital and one of the S_π orbitals, viewed perpendicular to the S_4 axis (note in this view the α-carbon is behind the sulfur and has been omitted for clarity). (c) Increased overlap between the Fe-($d_{x^2-y^2}$) orbital and one of the off-axis S_σ orbitals, viewed down the S_4 axis.

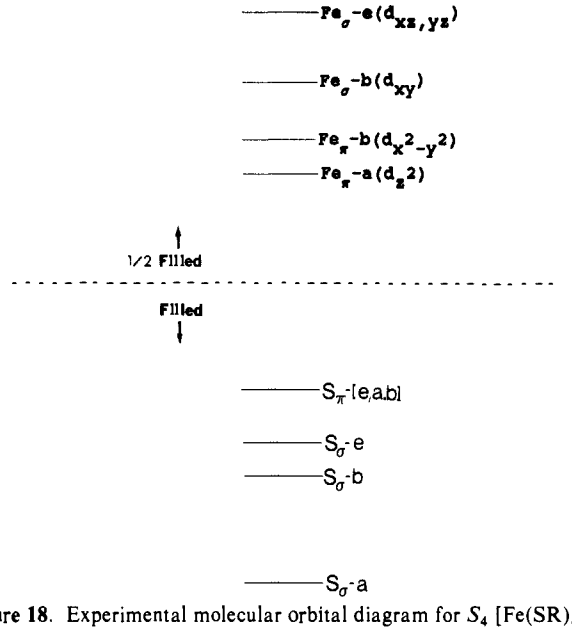

Figure 18. Experimental molecular orbital diagram for S_4 $[Fe(SR)_4]^-$.

Table IV

S(π) orbitals
S_π-a = $(-^1/_2)(S(\pi)_1 - S(\pi)_2 - S(\pi)_3 + S(\pi)_4)$
S_π-b = $(-^1/_2)(S(\pi)_1 + S(\pi)_2 + S(\pi)_3 + S(\pi)_4)$
S_π-e(x) = $(-^1/_2)(S(\pi)_1 + S(\pi)_2 - S(\pi)_3 - S(\pi)_4)$
S_π-e(y) = $(-^1/_2)(S(\pi)_1 - S(\pi)_2 + S(\pi)_3 - S(\pi)_4)$
S(σ) orbitals
S_σ-a = $(^1/_2)(S(\sigma)_1 + S(\sigma)_2 + S(\sigma)_3 + S(\sigma)_4)$
S_σ-b = $(^1/_2)(S(\sigma)_1 - S(\sigma)_2 - S(\sigma)_3 + S(\sigma)_4)$
S_σ-e(x) = $(-^1/_2)(S(\sigma)_1 - S(\sigma)_2 + S(\sigma)_3 - S(\sigma)_4)$
S_σ-e(y) = $(-^1/_2)(S(\sigma)_1 + S(\sigma)_2 - S(\sigma)_3 - S(\sigma)_4)$
$S(\sigma)_i$ is the 3p-σ S orbital centered on S_i, and $S(\pi)_i$ is the 3p-σ S orbital centered on S_i.

From Figure 18, there are 10 one-electron ligand to metal charge-transfer transitions that can give rise to electric dipole allowed x,y-polarized ^6E states. All of these must involve an e orbital as either the donor or the acceptor. The possible states

are as follows: S_σ-a → Fe_σ-e($d_{xz,yz}$), S_σ-b → Fe_σ-e($d_{xz,yz}$), S_σ-e → Fe_σ-b(d_{xy}), S_σ-e → Fe_π-b($d_{x^2-y^2}$), S_σ-e → Fe_π-a(d_{z^2}), S_π-e → Fe_σ-b(d_{xy}), S_π-b → Fe_σ-e($d_{xz,yz}$), S_π-a → Fe_σ-e($d_{xy,yz}$), S_π-e → Fe_π-a(d_{z^2}), and S_π-e → Fe_π-b($d_{x^2-y^2}$). There are eight possible one-electron ligand to metal charge-transfer transitions that give rise to electric dipole allowed z-polarized ^6B states: S_σ-a → Fe_σ-b(d_{xy}), S_σ-e → Fe_σ-e($d_{xz,yz}$), S_σ-a → Fe_π-b($d_{x^2-y^2}$), S_σ-b → Fe_π-a(d_{z^2}), S_π-a → Fe_σ-b(d_{xy}), S_π-e → Fe_σ-e($d_{xz,yz}$), S_π-b → Fe_π-a(d_{z^2}), and S_π-a → Fe_π-b($d_{x^2-y^2}$). From the polarized absorption spectrum (Figure 9), only four x,y-polarized ^6E (bands A, B, D, and F) and two z-polarized ^6B (bands C and E) transitions are observed. Clearly, some of the group theoretically allowed transitions predicted above are not very intense due to poor overlap[48] with the metal d orbitals. In particular, it is expected that S_σ → Fe_{σ^*} transitions will have the highest intensity due to strong overlap. S_π → Fe_{π^*} transitions should be less intense, and S_σ → Fe_{π^*} or S_π → Fe_{σ^*} transitions should be much weaker, but can have nonzero intensity because the S_σ valence orbitals have some limited S_π character due to the rotation of the σ bonding ligand orbital off the S–Fe bond (Figure 17).

All spin-forbidden transitions to quartet states have transition dipole moments that depend on the M_s sublevel of the ground state (Table II). Thus, all spin-forbidden transitions will show a temperature-dependent intensity due to population changes in the ZFS ground-state doublets. A lack of temperature dependence between 50 and 5 K is a strong indication that the transition is to a spin-allowed charge-transfer state.

Band A shows no change in intensity between 30 and 4.2 K, and therefore must be a charge-transition transition. Band A is highly x,y polarized (Figure 8), requiring a ^6E assignment. The low intensity relative to the higher energy charge-transfer transitions (bands B etc.) strongly indicates this state arises from a S_π → Fe_{π^*} charge-transfer transition.

The set of intense transitions (B–F) of Figure 9 are certainly spin-allowed ligand to metal charge-transfer transitions. There are five possible S_σ → Fe_{σ^*} transitions: two to z-polarized ^6B states [S_σ-a → Fe_σ-b(d_{xy}) and S_σ-e → Fe_σ-e($d_{xz,yz}$)], and three to x,y-polarized ^6E states [S_σ-a → Fe_σ-e($d_{xz,yz}$), S_σ-b → Fe_σ-e($d_{xz,yz}$), and S_σ-e → Fe_σ-b(d_{xy})]. Based on the high intensities of bands B–Fe (Figure 9) these can be assigned as the five S_σ → Fe_{σ^*} transitions. Band G exhibits mixed polarizations, which is not characteristic of either a ^6E or ^6B electric dipole allowed charge-transfer state and will be shown to be a ligand-centered transition.

(ii) Magnetic Circular Dichroism. (1) Single-Crystal Spectrum. For a molecule oriented with the magnetic field parallel to the z axis, only transitions that have x,y-polarized absorption intensity can be MCD active.[39] Therefore, in the absence of spin–orbit coupling only transitions to ^6E states can exhibit an MCD signal (i.e., temperature-independent A term). Spin–orbit coupling provides a mechanism for transitions to ^6E states to give rise to a temperature-dependent pseudo-A term. In addition, ^6B and ^6A excited states can gain x,y-polarized intensity by spin–orbit coupling with the ^6E states, producing C terms.

The ^6E states will exhibit an in-state spin–orbit splitting of the 12-fold degenerate ^6E into six equally spaced doubly dengerate states (3E′ and 3E″ in the S_4 double group). The energy spacing between the doublets is $(^1/_5)\lambda$, where λ is the multielectron spin–orbit coupling constant. The in-state spin–orbit splitting of a ^6E with a positive λ is presented in Figure 19 along with the wave functions in the uncoupled representation. The magnitude of λ depends on the specific doubly degenerate (e) molecular orbitals involved in the transition, while the sign depends only on the symmetry of the nondegenerate orbital [a(−) or b(+)]. The magnitude of λ is given by eq 4. The reduced matrix element

$$|\lambda| = (^2/_5)^{1/2}(\langle e||H_{so}||e\rangle) = (^2/_5)^{1/2}(\bar{\zeta}) \quad (4)$$

is the in-state spin–orbit coupling present in the doubly degenerate

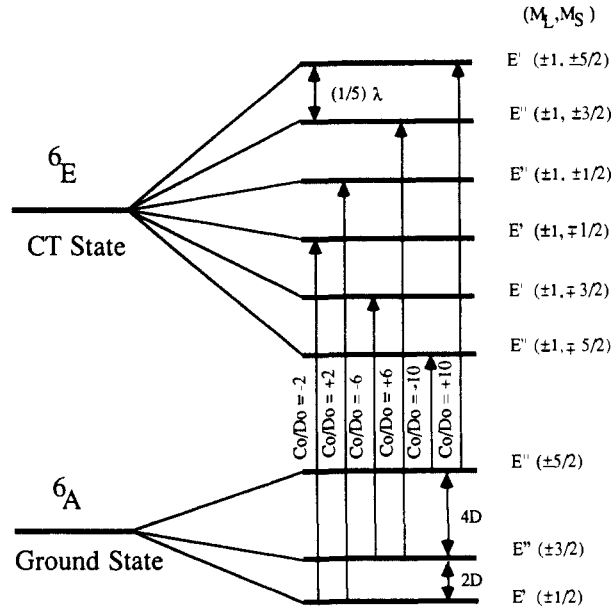

Figure 19. ^6E excited-state in-state spin–orbit splitting along with the wave functions and the theoretical C_0/D_0 ratios for transitions from the ZFS split ground-state levels to the spin–orbit components of the ^6E. The ZFS of the ground state is not drawn to scale.

one-electron orbital |e⟩, which is either the donor or the acceptor in the transition. $\bar{\zeta}$ is the effective one-electron spin–orbit coupling constant. If the wave functions, |e⟩, are pure Fe^{3+} 3d orbitals, then $\bar{\zeta}$ = 430 cm^{-1}.

The wave functions, |e⟩, in the above matrix element are in fact multicenter functions, with both metal and ligand SALC contributions. Since spin–orbit coupling is a localized one-center operator, contributions that occur between different centers can be neglected. In addition, the sulfur contribution[50] to spin–orbit coupling will be small due to the splitting of the degeneracy of the S 3p orbitals by the bonding to the phenyl ring and the iron. Therefore, only the metal character present in |e⟩ should contribute significantly to the magnitude of λ.

For a molecule oriented such that the magnetic field is parallel to the molecular z axis, the MCD signal is described[39] by eq 5.

$$(\Delta A/E) = \gamma C_0 \mu_B B f(E)/kT \quad (5)$$

γ depends on constants such as the dielectric constant and refractive index, μ_B is the Bohr magneton, B is the external magnetic field, $f(E)$ is an energy-dependent band-shape function, and C_0 is given eq 6. a and j are components of the irreducible repre-

$$C_0 = (-1/|A|)\sum_{a,j}\langle Aa|L_z + 2S_z|Aa\rangle x(|\langle Aa|m_{-1}|Jj\rangle|^2 - |\langle Aa|m_{+1}|Jj\rangle|^2) \quad (6)$$

sentations A (ground state) and J (excited state), $|A|$ is the total degeneracy of the ground state ($|A|$ = 6), and $\langle Aa|m_{\pm1}|Jj\rangle$ is the dipole matrix element for absorption of right (+) or left (−) circularly polarized light. The absorption intensity is given by eqs 7 and 8. By use of eq 17.2.25 of Piepho and Schatz[41] (p 365)

$$(A/E) = \gamma D_0 \quad (7)$$

$$D_0 = (^1/_2|A|)\sum_{a,j}(|\langle Aa|m_{-1}|Jj\rangle|^2 + |\langle Aa|m_{+1}|Jj\rangle|^2) \quad (8)$$

for the S_4 double group, the C_0/D_0 ratio for transitions from the E′ or E″ ground-state component to either a E″ or E′ excited state is given by

$$C_0/D_0 = \pm(8)^{1/2}\langle A||S_z||A\rangle \quad (9)$$

The plus applies for an E″ excited state, while the minus sign applies for an E′ excited state, and

$$\langle A||S_z||A\rangle = \pm(2)^{1/2}|M_s| \quad (10)$$

(48) Avoird, A.; Ros, P. *Theor. Chim. Acta* **1966**, *4*, 13.

(49) The 3p orbitals on the sulfur are substantially split by the α-C and the Fe d orbitals, therefore in-state orbital angular momentum is quenched. However, there is out-of-state contribution to spin–orbit coupling, but this will be small (<10 cm^{-1}).

(50) Schatz, P. N.; Mowery, R. L.; Krausz, E. R. *Mol. Phys.* **1978**, *35*, 1537.

The plus applies for the $M_s = \pm^1/_2$ or $\pm^3/_2$ ground-state sublevel while the minus applies for the $M_s = \pm^5/_2$ sublevel.

If the spin–orbit components could be resolved, the MCD signal would appear as two sets of three C terms with the following relative magnitudes, 5:3:1:−1:−3:−5. The sign of the highest energy C term depends on the sign of the spin–orbit splitting. When the bandwidth is much larger than the spin–orbit splitting, as is the case for this complex, the MCD signal will appear as a derivative-shaped temperature-dependent pseudo-A term.

The first moment of the MCD signal from a pair of C terms (J_1 and J_2) of equal magnitude but opposite sign whose bandwidths are much greater than the splitting, W, between them is given by eq 11. $W = E(J_2) - E(J_1)$, $C_0(J_2)$ is for state J_2, μ_B is the Bohr

$$\langle \Delta A/E \rangle_1 = \gamma C_0(J_2) W \mu_B B/kT \qquad (11)$$

magneton, and B is the external magnetic field. The 0th moment for the absorption due to these two states is given by eq 12. $D_0(J_2)$

$$\langle A/E \rangle_0 = 2\gamma[D_0(J_2)] \qquad (12)$$

is for the J_2 state. Combining eq 11 and eq 12 gives eq 13.

$$(\langle \Delta A/E \rangle_1)/(\langle A/E \rangle_0) = [C_0(J_2)/2D_0(J_2)] W \mu_B B/kT \qquad (13)$$

For the tetrathiolate system the situation is somewhat more complicated because the ^{6}E states are composed of the six overlapping spin–orbit components; however, this simplifies because the states appear as pairs split about a common center (Figure 19). The first moment for the MCD signal is the sum of the first moments for each of the three pairs of C terms as given in eq 14.

$$\langle \Delta A/E \rangle_1 = \textstyle\sum_i \gamma P_i C_0(J_2)_i W_i \mu_B B/kT \qquad (14)$$

P_i represents a population weighting taking into account the fact that transitions to each pair of spin–orbit components is allowed (Figure 19) from only one sublevel of the ground state, and

$$W_i = \lambda(^2/_5)(|M_s|) \qquad (15)$$

where M_s is the spin-state component coupled into the excited orbital angular momentum (Figure 19). P_i is defined so that the sum over the three ground-state doublets is 1. The 0th moment (eq 16) of the corresponding absorption band can be approximated as the sum of the moments of six absorption bands arising from the six spin–orbit components of the ^{6}E state.

$$\langle A/E \rangle_0 = \textstyle\sum_i \gamma P_i 2[D_0(J_2)_i] \qquad (16)$$

Since $D_0(J_2)_i$ is the same for all i, $\langle A/E \rangle_0 = 2\gamma[D_0(J_2)]$. This leads to the following expression for the ratio of the first moment of the MCD to the 0th moment of the absorption:

$$(\langle \Delta A/E \rangle_1)/(\langle A/E \rangle_0) = (\mu_B B/2kT) \textstyle\sum_i P_i [C_0(J_2)/D_0(J_2)]_i W_i \qquad (17)$$

where the sum is over the three pairs of spin–orbit states. By use of eq 15 for W_i and the values of the C_0/D_0 obtained above

$$(\langle \Delta A/E \rangle_1)/(\langle A/E \rangle_0) = (\lambda \mu_B B/5kT)[1 + 9\exp(-2D/kT) + 25\exp(-6D/kT)]/Q \qquad (18)$$

where $Q = [1 + \exp(-2D/kT) + \exp(-6D/kT)]$, λ is the spin–orbit coupling reduced matrix element for a ^{6}E state (eq 3), and D is the ZFS. When eq 18 is evaluated at 80 K and 60 kG, using $D = +2.4$ cm^{-1}, the following simple, but important result is obtained.

$$(\langle \Delta A/E \rangle_1)/(\langle A/E \rangle_0) \approx 0.102\lambda \qquad (19)$$

Thus measurement of the first moment of the MCD and the 0th moment of the corresponding absorption band allows an estimate of the in-state spin–orbit splitting in the excited state. This provides important insight into assignment of the one-electron orbitals involved in the $^6A \rightarrow {}^6E$ transition. Table I contains the moments for the three pseudo-A terms (band B, D, and F) observed in the MCD at 80 K and 60 kG. Also listed are the corresponding absorption moments. These are used to obtain λ and, from eq 4, the one-electron spin–orbit coupling constants (ζ) for each transition.

With light propagating down the c crystallographic axis, transitions to ^{6}A or ^{6}B states have no MCD activity due to the lack of x,y-polarized absorption intensity. However, these states will spin–orbit couple to the electric dipole allowed ^{6}E states gaining MCD C-term activity. For a spin–orbit coupling intensity-gaining mechanism the x,y-polarized transition moment for a transition from a component of the ^{6}A ground state to a component of the ^{6}B excited state is given by eq 20. H_{so} is the

$$\langle {}^6\mathrm{A}M_s|m_{x,y}|{}^6\mathrm{B}M_s'\rangle = \textstyle\sum_i (\langle {}^6\mathrm{E}_i h M_s|H_{so}|{}^6\mathrm{B}M_s'\rangle \langle {}^6\mathrm{A}M_s|m_{x,y}|{}^6\mathrm{E}_i h M_s\rangle)/[E({}^6\mathrm{E}_i)] \qquad (20)$$

spin–orbit coupling operator, $m_{x,y}$ is the electric dipole operator, and $E(^6E_i)$ is the energy separation between the ith ^{6}E state and the ^{6}B excited state. The expression for x,y-polarized intensity of ^{6}A states is analogous, differing only in phase. Application of the irreducible tensor method[41] to eq 20 yields eq 21, where

$$\langle {}^6\mathrm{A}M_s|m_{\pm 1}|{}^6\mathrm{B}M_s'\rangle = R\left(\begin{bmatrix} ^5/_2 & 1 & ^5/_2 \\ -M_s & \pm 1 & M_s' \end{bmatrix}\right) \times (^1/_2)^{1/2} \qquad (21)$$

$R = \sum_i (\langle {}^6\mathrm{E}_i||H_{so}||{}^6\mathrm{B}\rangle \langle {}^6\mathrm{A}||m||{}^6\mathrm{E}_i\rangle)/[E({}^6\mathrm{E}_i)]$. In eq 21 the complex basis is employed to faciliate calculation of MCD parameters. For a ^{6}B state eq 21 combined with eq 6 gives $C_0 = R/36$, $D_0 = R/72$, and $C_0/D_0 = 2$. Thus, a small amount of x,y-polarized intensity mixed into the ^{6}B state yields a significant MCD signal. Analogously, for ^{6}A excited states $C_0/D_0 = -2$. This mechanism accounts for the four [two positive (bands C and E) and two negative (bands M_3 and M_4)] C terms observed in the single-crystal MCD. The two positive C terms must result from ^{6}B states and therefore should correspond to z-polarized absorption bands (C and E), as is observed experimentally. The two negative C terms must result from ^{6}A states, which will have very low x,y-polarized absorption intensity as this derives from out-of-state spin–orbit coupling with electric dipole allowed states and should not contribute significantly to the polarized absorption spectrum.

(2) Mull Spectrum. The striking feature of the mull MCD spectrum (Figures 13 and 14) is the difference from the single-crystal MCD spectrum. For a purely x,y-polarized transition there can be no qualitative difference between the MCD of an oriented single crystal or an orientationally averaged mull sample.[50] There should only be a decrease of the orientationally averaged MCD signal by a factor of 3. Any differences in the two types of spectra must result from z-polarized absorption intensity.

In the region of the 12900-cm^{-1} absorption band (A) it is observed that the mull MCD signal changes sign from the single-crystal MCD, giving further evidence that the MCD signal (band M_1) actually derives from a z-polarized absorption band and not the x,y-polarized absorption band (A).

In the energy region from 15 000 to 19 000 cm^{-1} of Figure 13 two MCD signals not prominent in the single-crystal MCD spectrum dominate the mull spectrum. The positive MCD feature (band M_2) at 15 800 cm^{-1} is new and must result from a weak z-polarized band, as there is no evidence for a state at this energy in the z-polarized absorption spectrum (Figure 9). The negative MCD feature at 17 550 cm^{-1} corresponds to band C in the z-polarized absorption spectrum (Figure 9) and the positive single-crystal MCD feature (Figure 11). The fact that band C changed sign in the mull MCD is consistent with its z-polarized nature (Figure 9).

(iii) Assignment of Charge-Transfer States. Band G (Figure 9) shows no temperature dependence in the single-crystal MCD spectrum. For a ^{6}A ground state, MCD C-term behavior can only arise through spin–orbit coupling. The lack of C-term behavior indicates that spin–orbit coupling is negligible for this state. This will only occur if the donor and acceptor orbitals in the transition have virtually no metal character; thus, band G is dominantly ligand centered. The transition is present in the Fe complex but not the Ga analogue or the free ligand. It could be a forbidden transition in the free ligand that gets enhanced and red shifted upon interaction with Fe(III).

Band F is pure x,y polarized and must be a ^{6}E charge-transfer state and is the highest energy ligand to metal charge-transfer state. In addition, this band gives rise to a negative pseudo-A term

Table V

band	energy cm^{-1}	pol abs	MCD sin, crys	MCD mull	assignment
A	12900	x,y			$^6E(S_\pi\text{-e} \rightarrow Fe_\pi\text{-b}(d_{x^2-y^2})$ or $S_\pi\text{-e} \rightarrow Fe_\pi\text{-a}(d_{z^2}))$
M_1	13100	z	+C[a]	-C	$^6B(S_\pi\text{-a} \rightarrow Fe_\pi\text{-b}(d_{x^2-y^2})$ or $S_\pi\text{-b} \rightarrow Fe_\pi\text{-a}(d_{z^2}))$
M_2	15800	z		+C	$^6B(\pi \rightarrow \sigma^*$ or $\sigma \rightarrow \pi^*)$
B	17000	x,y	+PA[b]		$^6E(S_\sigma\text{-e} \rightarrow Fe_\sigma\text{-b}(d_{xy}))$
C	17500	z	+C	+C	$^6B(S_\sigma\text{-e} \rightarrow Fe_\sigma\text{-e}(d_{xz,yz}))$
M_3	18700				$^6A(S_\sigma\text{-b} \rightarrow Fe\text{-b}(d_{xy})$ or $S_\sigma\text{-e} \rightarrow Fe_\sigma\text{-e}(d_{xz,yz}))$
M_4	20300				$^6A(S_\sigma\text{-a} \rightarrow Fe_\pi\text{-a}(d_{z^2}))$
D	20650	x,y	+PA		$^6E(S_\sigma\text{-b} \rightarrow Fe_\sigma\text{-e}(d_{xz,yz}))$
E	22450	z	+C		$^6B(S_\sigma\text{-a} \rightarrow Fe_\sigma\text{-b}(d_{xy}))$
F	24900	x,y	-PA		$^6E(S_\sigma\text{-a} \rightarrow Fe_\sigma\text{-e}(d_{xz,yz}))$
G	29000	mixed[d]	+B[c]		intraligand

[a] *C* term. [b] Pseudo-*A* term. [c] *B* term. [d] $x,y/z \approx 3.5$.

MCD signal and thus must arise from a $S_\sigma\text{-a} \rightarrow Fe_\sigma\text{-e}(d_{xz,yz})$, $S_\sigma\text{-e} \rightarrow Fe_\pi\text{-a}(d_{z^2})$, $S_\pi\text{-a} \rightarrow Fe_\sigma\text{-e}(d_{xz,yz})$, or $S_\pi\text{-e} \rightarrow Fe_\pi\text{-a}(d_{z^2})$ transition. On the basis of the relative magnitude ($\zeta = -250\ cm^{-1}$) of the effective spin–orbit coupling constant (Table I) this transition undoubtedly involves the metal $Fe_\sigma\text{-e}(d_{xz,yz})$ set as the acceptor orbital. The intensity of the transition ($\epsilon \approx 12000\ cm^{-1}\ M^{-1}$) is indicative of a $S_\sigma \rightarrow Fe_{\sigma^*}$ charge-transfer transition, and so band F must be assigned as the $S_\sigma\text{-a} \rightarrow Fe_\sigma\text{-e}(d_{xz,yz})$ transition.

Band E is purely *z* polarized, indicating it is a ^6B charge-transfer state. There are several possible one-electron transitions that will give rise to a ^6B state; however, on the basis of the large intensity of the transition, it undoubtedly arises from a $S_\sigma \rightarrow Fe_{\sigma^*}$ transition leaving only a $S_\sigma\text{-a} \rightarrow Fe_\sigma\text{-b}(d_{xy})$ or $S_\sigma\text{-e} \rightarrow Fe_\sigma\text{-e}(d_{xz,yz})$ as possibilities. Band E is observed at 2500 cm^{-1} below band F, which is assigned above as the $S_\sigma\text{-a} \rightarrow Fe_\sigma\text{-e}(d_{xz,yz})$ transition. This energy difference is close to the splitting observed for the Fe d orbitals [$Fe_\sigma\text{-e}(d_{xz,yz})$ and $Fe_\sigma\text{-b}(d_{xy})$] (Figure 16). On the basis of this, band E is assigned as the $S_\sigma\text{-a} \rightarrow Fe_\sigma\text{-b}(d_{xy})$ transition.

Band D is purely *x,y* polarized and exhibits a positive pseudo-*A* term MCD signal. It must arise from a $S_\sigma\text{-b} \rightarrow Fe_\sigma\text{-e}(d_{xz,yz})$, $S_\sigma\text{-e} \rightarrow Fe_\sigma\text{-b}(d_{xy})$, $S_\sigma\text{-e} \rightarrow Fe_\pi\text{-b}(d_{x^2-y^2})$, $S_\pi\text{-b} \rightarrow Fe_\sigma\text{-e}(d_{xz,yz})$, $S_\pi\text{-e} \rightarrow Fe_\sigma\text{-b}(d_{xy})$, or $S_\pi\text{-e} \rightarrow Fe_\pi\text{-b}(d_{x^2-y^2})$ transition. Band D has an effective spin–orbit splitting of magnitude (Table I) similar to band F, indicating that the $Fe_\sigma\text{-e}(d_{xz,yz})$ orbitals are involved in the transition. On the basis of this and the high intensity of the transition, which favors an $S_\sigma \rightarrow Fe_{\sigma^*}$ assignment, band D is assigned as the $S_\sigma\text{-b} \rightarrow Fe_\sigma\text{-e}(d_{xz,yz})$ transition.

Band C is *z* polarized and can arise from six possible one-electron transitions [$S_\sigma\text{-e} \rightarrow Fe_\sigma\text{-e}(d_{xz,yz})$, $S_\sigma\text{-a} \rightarrow Fe_\pi\text{-b}(d_{x^2-y^2})$, $S_\sigma\text{-b} \rightarrow Fe_\pi\text{-b}(d_{z^2})$, $S_\pi\text{-e} \rightarrow Fe_\sigma\text{-e}(d_{xz,yz})$, $S_\pi\text{-a} \rightarrow Fe_\sigma\text{-b}(d_{xy})$, or $S_\pi\text{-a} \rightarrow Fe_\pi\text{-b}(d_{x^2-y^2})$]. On the basis of the relatively high intensity of this transition, the most plausible assignment for band C is the $S_\sigma\text{-e} \rightarrow Fe_\sigma\text{-e}(d_{xz,yz})$ transition.

Band B is a purely *x,y*-polarized ^6E state and is associated with a positive pseudo-*A* term in the MCD spectrum. The spin–orbit splitting of band B is roughly half the magnitude of bands D and F, leading to the conclusion that the doubly degenerate orbital set involved in the transition is not the $Fe_\sigma\text{-e}(d_{xz,yz})$ set. This leaves four possibilities for the transition: $S_\sigma\text{-e} \rightarrow Fe_\sigma\text{-b}(d_{xy})$, $S_\sigma\text{-e} \rightarrow Fe_\pi\text{-b}(d_{x^2-y^2})$, $S_\pi\text{-e} \rightarrow Fe_\sigma\text{-b}(d_{xy})$, or $S_\pi\text{-e} \rightarrow Fe_\pi\text{-b}(d_{x^2-y^2})$. The S_π-e ligand set is not expected to have appreciable metal character, should not produce a measurable in-state spin–orbit splitting, and therefore can be ruled out. The S_σ-e ligand SALC should have significant mixing with the $Fe_\sigma\text{-e}(d_{xz,yz})$ orbitals and is most likely involved in the transition. In addition, the intensity of this band supports a $S_\sigma \rightarrow Fe_{\sigma^*}$ assignment. Thus, band B is assigned as the $S_\sigma\text{-e} \rightarrow Fe_\sigma\text{-b}(d_{xy})$ transition.

Band A is a *x,y*-polarized ^6E state (Figure 9). In contrast to the higher energy ^6E states (bands B, D, and F), band A has no pseudo-*A* term MCD signal associated with it. The in-state spin–orbit splitting of this band must be negligible, indicating a lack of metal character in the e orbital involved in the transition. The ligand S_π-e set is favored because it is the only weakly bonding e orbital and should have minimal metal d orbital character. Band A is most reasonably assigned as either the $S_\pi\text{-e} \rightarrow Fe_\pi\text{-a}(d_{z^2})$ or $S_\pi\text{-e} \rightarrow Fe_\pi\text{-b}(d_{x^2-y^2})$ transitions. The relatively low intensity ($\epsilon = 340\ M^{-1}\ cm^{-1}$) is consistent with the observation that the transition involves weakly overlapping π orbitals.

On the basis of the positive MCD signal, band M_1 is a ^6B charge transfer state. Band M_1 must be a *z*-polarized transition, but based on the lack of a transition in the *z*-polarized absorption spectrum (Figure 8), it must have an $\epsilon < 30\ M^{-1}\ cm^{-1}$. On the basis of the other assignments, the energy of band M_1 is too low for an assignment as either a $S_\sigma \rightarrow Fe_{\pi^*}$ or $S_\pi \rightarrow Fe_{\sigma^*}$ (Figure 18). Band M_1 is therefore assigned as an $S_\pi \rightarrow Fe_{\pi^*}$ transition [$S_\pi\text{-a} \rightarrow Fe_\pi\text{-b}(d_{x^2-y^2})$ or $S_\pi\text{-b} \rightarrow Fe_\pi\text{-a}(d_{z^2})$]. Band M_2 (Figure 14) is only evident in the mull MCD and so must arise from a *z*-polarized transition. This has an energy consistent with a $\sigma \rightarrow \pi^*$ or $\pi \rightarrow \sigma^*$ transition (Figure 18). Based on this and the low absorption intensity, the most plausible assignment is as the $S_\pi\text{-e} \rightarrow Fe_\sigma\text{-e}(d_{xz,yz})$, $S_\sigma\text{-a} \rightarrow Fe_\pi\text{-b}(d_{x^2-y^2})$, or $S_\sigma\text{-b} \rightarrow Fe_\pi\text{-a}(d_{z^2})$ transition. Bands M_3 (18700 cm^{-1}) and M_4 (20300 cm^{-1}) are not evident in the polarized absorption spectra, but are required by the single-crystal MCD spectrum (Figure 12). Both of these transitions exhibit negative *C* terms in the single-crystal MCD spectrum. These states arise from transitions to ^6A states. These transitions are electric dipole forbidden and to first order will have no absorption intensity. On the basis of the energies for the other charge-transfer bands, M_3 is assigned as either the $S_\sigma\text{-b} \rightarrow Fe_\sigma\text{-b}(d_{xy})$ or the $S_\sigma\text{-e} \rightarrow Fe_\sigma\text{-e}(d_{xz,yz})$ transition, while band M_4 is most likely the $S_\sigma\text{-a} \rightarrow Fe_\pi\text{-a}(d_{z^2})$ transition.

The energies, absorption, and MCD properties and assignments of bands A–G and M_1–M_4 are summarized in Table V and Figure 20. By use of the assignment of the observed charge-transfer bands, an experimental one-electron ligand molecular orbital energy order is obtained (Figure 18). The energies of the orbitals in Figure 18 assume no relaxation due to changes in electron repulsion occurs upon electron excitation. While this is not strictly correct, the correction for each charge-transfer state should be similar. Therefore, Figure 18 represents a reasonable description of the energy ordering of the ligand and metal molecular orbitals.

(c) Origin of Zero-Field Splitting in $Fe(SR)_4$. There are two mechanisms that contribute to the ZFS of the $^6A_1$ ground state of axially distorted HS d^5 transition-metal ions. These are spin–spin coupling within the ground state and spin–orbit coupling to low-symmetry-split excited states. The spin–spin contribution has been estimated[36] to be on the order of $10^{-3}\ cm^{-1}$ and positive. Typical ZFS splittings in Fe(III) complexes are much larger, so this contribution can be neglected. Thus, the spin–orbit mechanism is the dominant contribution to the ZFS. Griffith[51] developed a model to explain the ZFS observed in axially distorted HS d^5

(51) (a) Griffith, J. S. *Biopolym. Symp.* **1964**, *1*, 35. (b) Griffith, J. S. *Mol. Phys.* **1964**, *8*, 213.

(52) Note than an additional complication arsies in the analysis of the ZFS in terms of spin-unrestricted Xα calculations. As the wave functions obtained from these calculations are not eigenfunctions of the spin operator, the spin-polarized wave functions cannot be used with eq 23 and 24. However, the sign of *D* must still arise from the difference in the numerators of eq 23. The magnitude of spin–orbit coupling matrix elements in the spin-unrestricted formalism is proportional to the total spin density distribution, and this is similar in both the spin-restricted and -unrestricted calculations as it depends on the spin-down unoccupied wave functions. Thus, the general predictions of eqs 23 and 24 will still hold.

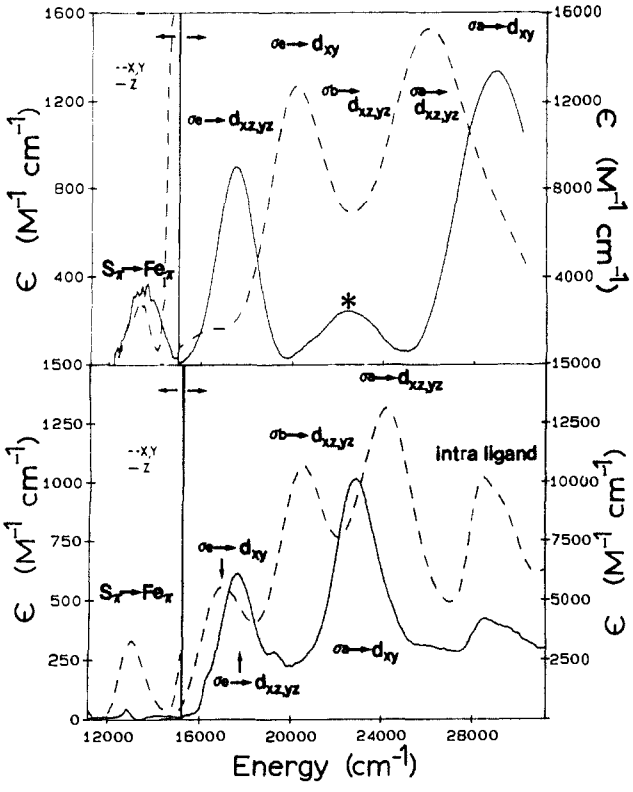

Figure 20. Single-crystal polarized absorption spectrum (top) and assignments for *Cp* rubredoxin as adapted from Eaton and Lovenberg (* this band is most likely an artifact of the process used to determine the molecular polarizations). Polarized absorption spectrum (101 face) of 0.05 mm thick $[NEt_4][Ga\{Fe\}(SR)_4]$ ([Fe] = 1%) at 6 K (bottom).

systems in terms of second-order spin–orbit coupling of the ground state to the axial symmetry split orbital components of the $^4T_1$ ligand field states. The Griffith model leads to the following equations for the contributions to D:

$$D(^4T_1^{a,c}) = (\zeta_{Fe^{3+}})^2[1/E_z - 1/E_{x,y}]/5 \quad (22a)$$

$$D(^4T_1^{b}) = (\zeta_{Fe^{3+}})^2[1/E_z - 1/E_{x,y}]/10 \quad (22b)$$

where $\zeta_{Fe^{3+}}$ is the Fe(III) spin–orbit coupling constant (430 cm^{-1}), and E_z and $E_{x,y}$ are the energies of the z and x,y components of the low-symmetry-split $^4T_1$ ligand field states. These equations are valid for the strong-field states [i.e., $^4T_1^a$ ($t_2^2e^3$), $^4T_1^b$ ($t_2^3e^2$), $^4T_1^c$ ($t_2^4e^1$)]. The total D is the sum of the contributions from the individual $^4T_1$ states. In the Griffith treatment D arises entirely from a difference in the energy denominators. The $^4T_1^a$ ($t_2^2e^3$) state is the first excited state and is much closer to the ground state than the third $^4T_1$ state. The second $^4T_1$ state will not be significantly low-symmetry split because it derives mostly from the ($t_2^3e^2$) configuration. Thus, the $^4T_1^a$ ($t_2^2e^3$) state gives the dominant contribution to D. Including the experimental energies of the $^4T_1^a$ orbital components (Table III) in eq 22a gives D = −0.7 cm^{-1}, while the experimentally observed D = +2.4 cm^{-1}. A similar disagreement in the predicted sign and magnitude of D was observed for D_{2d} distorted tetrahedral ferric tetrachloride.[37]

From our earlier work[37] on D_{2d} $FeCl_4^-$, the problem with the Griffith model arises from the neglect of covalency in eq 22. Covalency affects the ZFS in two ways. The most significant effect results from anisotropic covalency, which derives from differences in mixing of the Fe(III) d orbitals with the ligand orbitals. This results in differences in the magnitude of spin–orbit coupling between the ground state and each of the orbital components of the $^4T_1$ states. Inclusion of covalency also leads to a charge-transfer contribution to the ZFS that arises from $^6A_1$ spin–orbit coupling to $^6T_1$ charge-transfer states. The latter contribution also leads to a deviation of the g values from 2.0023 as is experimentally observed for the tetrathiolate complex.

From ref 37, inclusion of covalency in the metal σ antibonding d orbitals leads to modified versions of eq 22:

$$D(^4T_1^{a,c}) = (\zeta_{Fe^{3+}})^2[\kappa_z^2/E_z - \kappa_{x,y}^2/E_{x,y}]/5 \quad (23a)$$

$$D(^4T_1^{b}) = (\zeta_{Fe^{3+}})^2[\kappa_z^2/E_z - \kappa_{x,y}^2/E_{x,y}]/10 \quad (23b)$$

where

$$\kappa_z = (1 - \alpha^2)^{1/2}(1 - \beta^2)^{1/2} \quad (24a)$$

$$\kappa_{x,y} = (1 - \alpha^2)^{1/2}(1 - \gamma^2)^{1/2} \quad (24b)$$

κ_z and $\kappa_{x,y}$ are similar to Stevens orbital reduction factors[53] used in the interpretation of g values and depend on the degree of covalency of the one-electron Fe(III) d orbitals. α represents the amount of ligand character mixed into the d(π) [Fe_π-a(d_{z^2}) and Fe_π-b($d_{x^2-y^2}$)] orbitals, β the ligand character in the Fe_σ-b(d_{xy}) orbital, and γ the ligand character mixed into the Fe_σ-e($d_{xz,yz}$) orbitals. As long as the two d(π) orbitals can be treated as having similar covalent mixing, eq 23 is valid in D_{2d} symmetry. If the mixing between the Fe_π-b($d_{x^2-y^2}$) and Fe_σ-b(d_{xy}) orbitals is small, these expressions are also valid for an Fe(III) site with S_4 symmetry. With no covalency (i.e., $\alpha = \beta = \gamma = 0$) eq 23 reduces to eq 22. In T_d symmetry it is required that $\beta^2 = \gamma^2$, and thus $\kappa_{x,y} = \kappa_z$. In D_{2d} and S_4 symmetry this restriction is removed, and covalency differences in the one-electron d orbitals will cause $\kappa_{x,y} \neq \kappa_z$. Because $\kappa_{x,y}$ and κ_z enter in the numerators of eq 23, the ZFS is much more sensitive to differences in these parameters than to differences in the energy denominators ($E_{x,y}$ and E_z).

Anisotropic covalency in the σ antibonding Fe d orbitals [Fe_σ-b(d_{xy}) and Fe_σ-e($d_{xz,yz}$)] causes the contribution from the lowest ligand field $^4T_1^a$ to be reduced and the contribution from the third ligand field $^4T_1^c$ state to be enhanced. This can be understood as follows: From eq 3a the axial low symmetry splitting of the first ligand field $^4T_1^a$ state will be positive (i.e., $E_{x,y} > E_z$) if the Fe_σ-b(d_{xy}) orbital is at higher energy than the Fe_σ-e($d_{xz,yz}$) set. The same one-electron splitting causes the third ligand field $^4T_1^c$ to have a negative splitting. Since the d orbitals are antibonding, the higher energy d orbital should have the largest covalent interaction with the ligands. Therefore, if the Fe_σ-b(d_{xy}) orbital is above the Fe_σ-e($d_{xz,yz}$), then $\beta > \gamma$ and from eq 24, $\kappa_{x,y} > \kappa_z$. Thus the orbital reduction factors and energy denominators oppose each other for the $^4T_1^a$ state and enhance each other for the $^4T_1^c$ state. This means the $^4T_1^c$ contribution to D cannot be neglected, and in fact this state gives the dominant contribution to D. This effect is general and will always occur for axially distorted T_d HS d^5 complexes. The net result of this anisotropic covalency is to cause the calculated value of D to change sign from the predictions of the Griffith model (eq 22), as has been experimentally observed in both the $FeCl_4^-$ complex[37] and the Fe-$(SR)_4^-$ complex.

Greater covalency of the Fe_σ-b(d_{xy}) orbitals leads to a negative D, while greater covalency of the Fe_σ-e($d_{xz,yz}$) set gives a positive D. The positive D observed in the thiolate complex requires the Fe_σ-e($d_{xz,yz}$) set to be more covalent and thus should be energetically above the Fe_σ-b(d_{xy}) orbital. The ligand field analysis, based on the axial splitting of the $^4T_1^a$ and $^4T_2^a$ states, independently supports this analysis of D, as the Fe_σ-e($d_{xz,yz}$) orbitals are found to be 2700 cm^{-1} above the Fe_σ-b(d_{xy}) orbital (Figure 16).

Based on the spin-restricted SCF-Xα-SW calculations[24] on $Fe(SCH_3)_4^-$ the Fe_π, Fe_σ-b(d_{xy}), and Fe_σ-e($d_{xz,yz}$) orbitals are estimated to have 0.9, 0.9, and 0.55% metal character, respectively ($\alpha^2 = 0.1$, $\beta^2 = 0.1$, and $\gamma^2 = 0.45$). The energies of the two unobserved $^4T_1$ states ($^4T_1^{b,c}$) were estimated from the ligand field analysis (section a.iv of the analysis). Employing eq 23a,b, with a spin–orbit coupling constant of 430 cm^{-1} and the experimentally observed $^4T_1^a$, low-symmetry components D_{calc} = +1.02 cm^{-1}, while D_{exp} = +2.4 ± 0.1 cm^{-1}.

As noted above, covalency also results in a charge-transfer contribution to D. In the absence of covalency, $^6\Gamma$ charge-transfer

(53) Stevens, K. W. H. *Proc. R. Soc. London* **1953**, *A219*, 542.

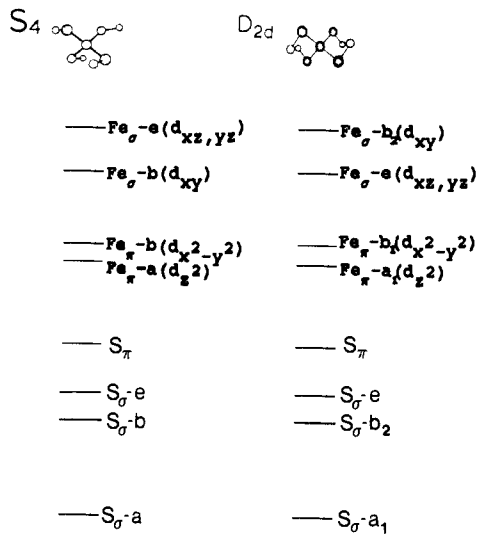

Figure 21. Qualitative molecular orbital diagrams comparing two axial geometries (D_{2d} and S_4) for $[Fe(SR)_4]^-$ complexes.

states cannot spin–orbit couple to the ground state. That this occurs is evident from the deviation of the experimental EPR g values from the free ion value of 2.0023. In T_d symmetry this can only result from a spin–orbit interaction between the $^6A_1$ ground state and T_1 states of the same spin. The only $^6T_1$ states available for spin–orbit coupling are the charge-transfer states. If this interaction is anisotropic it will also lead to a charge-transfer contribution to D. Theoretically, the $^6T_1$ charge-transfer contributions to D are difficult to calculate; however, this contribution can be determined experimentally through an accurate measurement of the anisotropy in the g values[37] (eq 25). The charge-transfer contribution to D is related to the g value anisotropy through eq 25.

$$D(^6T) = (\bar{\zeta})(g_{x,y} - g_z) \qquad (25)$$

$\bar{\zeta}$ is an effective one-electron spin–orbit coupling constant. By use of $\bar{\zeta} = 300$ cm^{-1} (reduced by 30% due to covalency), and the experimentally determined g value anisotropy of 0.005 ± 0.0002, the $^6T_1$ charge-transfer contribution to $D = +0.15 \pm 0.06$ cm^{-1}. Thus, the total $D_{calc} = +1.17$ cm^{-1}. Considering the approximations used in the above model, the factor of 2 difference from the experimental value appears to be reasonable. More importantly, the anisotropy covalency model provides a clear explanation for the positive sign and large magnitude of D in terms of increased covalency of the Fe$_\sigma$-e($d_{xz,yz}$) orbitals due to the orientation of the R group.[52]

Discussion

The combination of single-crystal polarized absorption and single-crystal and orientationally averaged MCD spectroscopies has provided a detailed understanding of the excited-state electronic structure of the $Fe(SC_6(CH_3)_4H)_4^-$ model complex. These excited-state features have been correlated to the ground-state ZFS as determined from single-crystal and orientationally averaged EPR. In addition, the assignment of the ligand field and charge-transfer spectrum has provided an experimental energy order for the ligand valence and Fe d orbitals (Figure 18).

A striking feature of the electronic structure of the $Fe(SR)_4^-$ complex is the low energy of the $^6A_1 \rightarrow {}^4T_1{}^a$, $^4T_2{}^a$, and $^4E^a$ d $\rightarrow$ d transitions (Table III), which occur roughly 6500 cm^{-1} lower in energy than the corresponding transitions in the D_{2d} distorted tetrahedral $FeCl_4^-$ complex.[37] Since the $^4E^a$ state arises from a spin flip of an electron in the t_2 orbital it is a ligand field independent state whose energy is only affected by electron repulsion differences between the ground and excited states. In the absence of covalency the $^4E^a$ state should occur at the free ion ^4G energy (32 000 cm^{-1}).[44] Experimentally,[45,54] covalency is found to reduce the energy of the $^4E^a$ state. In d^5 Mn(II) complexes[54] the $^4E^a$ state is found at 95–85% of the free ion ^4G. This can be compared to the more covalent $FeCl_4^-$ complex[37] where the $^4E^a$ state is found at 56% of the free ion ^4G. The $^4E^a$ transition in the $Fe(SR)_4^-$ complex occurs at 35% of the free ion energy, indicating substantially greater delocalization over the RS^- ligands relative to Cl^- ligands. The large reduction in electron repulsion also explains the low energy of the $^4T_1{}^a$ and $^4T_2{}^a$ states.[42] Ab initio Hartree–Fock calculations[22] performed on a $Fe(SH)_4^-$ complex by Bair and Goddard[22] indicated a highly delocalized bonding scheme with a set of low-energy d $\rightarrow$ d transitions predicted at $\sim$8000 cm^{-1}, a result that is now supported by experiment. A similar delocalized bonding scheme is observed from spin-unrestricted SCF–Xα–SW calculations[55] performed by Norman and Jackels[24] and by Noodleman[23] et al. on $Fe(SR)_4^-$ complexes. The high covalency is also consistent with the hyperfine coupling observed[17] in the Mössbauer spectrum.

The charge-transfer spectroscopy on $Fe(SR)_4^-$ has revealed that the region from 16 000 to 28 000 cm^{-1} is comprised solely of $S_\sigma \rightarrow Fe_{\sigma^*}$ charge-transfer states (Figure 20). The highest energy charge-transfer states are the S_σ-a $\rightarrow Fe_\sigma$ states, indicating that the S_σ-a orbital is stabilized the most upon binding to Fe. This stabilization must arise from its interaction with the Fe 4s orbital. The next set of charge-transfer states to lower energy are the S_σ-b and S_σ-e $\rightarrow Fe_\sigma$ states, with the S_σ-b level observed to be more stabilized because it interacts with two d orbitals [Fe$_\sigma$-b(d_{xy}) and Fe$_\pi$-b($d_{x^2-y^2}$)]. The S_π manifold is the least stabilized with no measurable energy splitting of the S_π-a,b,e levels.

The axial splitting pattern observed in the Fe d orbitals of the $Fe(SR)_4^-$ complex is reversed from the splitting pattern observed in the D_{2d} $FeCl_4^-$ complex[37] (Figure 16) even though the $Fe(S)_4$ core is structurally equivalent to the $FeCl_4^-$ geometry.[56] Both complexes have a D_{2d} distorted structure arising from a limited compression along the S_4 axis of the tetrahedron. In $FeCl_4^-$ the low-symmetry distortion causes the z components of both the $^4T_1{}^a$ and $^4T_2{}^a$ states to be at lower energy than their corresponding x,y partners, requiring the d_{xy} orbital to be above the $d_{xz,yz}$ orbital set by 1300 cm^{-1} and the $d_{x^2-y^2}$ to be 230 cm^{-1} below the d_{z^2} orbital. In contrast, for the thiolate model complex the Fe$_\sigma$-e($d_{xz,yz}$) set is found to be 2700 cm^{-1} above the Fe$_\sigma$-b(d_{xy}) orbital and the Fe$_\pi$-b($d_{x^2-y^2}$) orbital is 1200 cm^{-1} above the Fe$_\pi$-a(d_{z^2}) orbital (Figure 16). In addition, the sign of D is positive in the thiolate model complex, but negative in the chloride complex, indicating the opposite Fe$_\sigma$ anisotropic covalency pattern. This reversal of

(54) Jorgensen, C. K. *Prog. Inorg. Chem.* **1962**, *4*, 73.

(55) It should be noted that the spin-unrestricted Xα bonding description for high-spin ferric complexes is quite different from the traditional ligand field description. In the Xα description, the highest occupied molecular orbitals (spin-up) are localized mainly on the ligands while the lowest unoccupied molecular orbitals (spin-down) are localized mostly on the metal. This is in contrast to the standard ligand field spin-restricted scheme, which requires these two sets of orbitals to have equivalent spatial distributions mostly localized on the metal. It has recently been determined[61] by variable-energy photoelectron spectroscopy that this inverted bonding scheme provided by the spin-unrestricted calculations is in fact correct. This inverted bonding description might be expected to yield a qualitatively different set of bound-state transitions relative to the tradiational ligand field description; however, both have much in common. Both schemes describe the spin-allowed charge-transfer states as arising from transitions from spin-down mostly ligand bonding or nonbonding orbitals to spin-down mostly metal antibonding orbitals. Both describe the $^4\Gamma$ states as originating from transitions between spin-up and spin-down antibonding orbitals. The only difference being the amount of metal character present in the orbitals involved. Thus, the determination of the one-electron orbital splittings from the low-symmetry splitting of the multielectron excited states (eq 3) is equivalent in both schemes, with the only caveat being that in the spin-unrestricted formalism the magnitudes of the low-symmetry splittings of spin-up and spin-down orbitals are not required to be equal. In both descriptions the splitting between the $^4E^a$ and $^4T_{1,2}{}^a$ states reflect the magnitude of $10Dq$. The major difference between the two schemes is the explanation of the nature and energy of the spin-forbidden transitions, which have been described as d $\rightarrow$ d transitions in ligand field theory. In the spin-unrestricted description these low-energy $^6A_1 \rightarrow {}^4\Gamma$ transitions have significant charge-transfer character. This provides a clear explanation of the large reduction in the energy of the $^6A_1 \rightarrow$ ($^4E^a$, $^4T_1{}^a$, $^4T_2{}^a$) transitions on going from the Cl^- to the thiolate compelxes. This decrease directly reflects the difference in the valence ionization energies of these two ligands.[61]

(56) Cotton, F. A.; Murillo, C. A. *Inorg. Chem.* **1975**, *14*, 2467.

the splitting and covalency pattern must be due to the orientation of the R = $C_6(CH_3)_4H$ group on the ligand.

The R group α-C affects bonding interactions between the sulfur and the iron because it orients the 3p valence orbitals on the sulfur. Two parameters are needed to define the α-C orientation (dihedral angle[57] and Fe–S–C_α angle). It has been proposed[21] that the α-C dihedral angles influence on the S_π orbitals is responsible for the d orbital splitting pattern in rubredoxin. On the basis of the geometry of the $Fe(SR)_4^-$ model complex studied here [the dihedral angle is 90° and the Fe–S–αC angle is 102.4° (Figure 2)] the S_π orbital should have its greatest overlap with the Fe_σ-b(d_{xy}) and Fe_π-a(d_{z^2}) orbitals (Figure 17b), causing these orbitals to be energetically above their tetrahedral partners. Also, if S_π bonding was dominant, the S_4 splitting between the Fe_π set should be larger than the S_4 splitting between the Fe_σ orbital set. Experimentally, the opposite S_4 splitting pattern is observed, which indicates that π bonding is not dominant in this complex. Additional evidence for a small S_π interaction comes from the relatively weak intensity (ϵ = 340 M^{-1} cm^{-1}) of the $S_\pi \rightarrow Fe_\pi$ transition (band A), which can be contrasted to the intensity of the thiolate $S_\pi \rightarrow Cu_\pi(d_{x^2-y^2})$ transition in blue copper proteins[58] (ϵ = 4000 M^{-1} cm^{-1}) where the S_π bonding with the $Cu(d_{x^2-y^2})$ orbital is significant. The intensity[48] of a charge-transfer transition is correlated to the amount of common ligand orbital character in the orbitals involved in the transition, indicating little S_π character in the Fe_π orbitals. Also, the lack of a measurable in-state spin–orbit splitting in band A ($|\zeta| < 20$ cm^{-1}), indicates negligible Fe_σ-e($d_{xz,yz}$) character in the S_π-e orbital.

The position of the α-C also affects the orientation of the S_σ orbitals. As seen in Figure 17a, the Fe–S–C_α angle of 102° rotates the S_σ orbital off the Fe–S bond, while leaving it in the Fe–S–C_α plane. As the pseudo-S_σ orbital is rotated off the bond its overlap with the Fe_σ-b(d_{xy}) orbital will decrease; however, the overlap with the Fe_σ-e($d_{xz,yz}$) orbital set remains unchanged (the overlap will increase for two ligands but decrease for the other two). This results in the Fe_σ-e($d_{xz,yz}$) orbital set being at higher energy and more covalent than the Fe_σ-b(d_{xy}) orbital, as is observed experimentally (Figure 16). Rotation of the S_σ orbital off the Fe–S bond will increase overlap with the Fe_π-b($d_{x^2-y^2}$) orbital (Figure 17c) while decreasing any overlap with the Fe_π-a(d_{z^2}) orbital. This is also consistent with the experimentally observed splitting. Therefore, it is the off-axis orientation of the S_σ orbitals, due to the C_α–S–Fe angle being greater than 90°, coupled with the dihedral angle that determines the dominant bonding interaction in this complex.

The D_{2d} thiolate geometry (Figure 21, right) with 180° dihedral angles must also be considered as it most closely represents the geometry of the active site of rubredoxin, and it is the geometry for which the SCF–Xα–SW calculations were performed. In this geometry the S_σ orbital has larger overlap with the Fe_σ-b_2(d_{xy}) relative to the Fe_σ-e($d_{xz,yz}$) orbitals. As with the S_4 complex, in the D_{2d} geometry the S_σ-a orbital will be the most stable bonding orbital due to Fe 4s bonding. In this geometry the splitting of the S_σ-e and S_σ-b_2 ligand levels should mirror the splitting of the corresponding d orbitals. Also, the Fe_π-b_1($d_{x^2-y^2}$) orbital will be above the Fe_π-a_1(d_{z^2}) because these orbitals are nonbonding with respect to the S_σ orbitals, and the Fe_π-a_1(d_{z^2}) orbital is nonbonding with respect to the S_π orbital. In this geometry the ZFS should be negative.[59] The SCF–Xα–SW calculations[23,24] on a $Fe(S-CH_3)_4^-$ complex were performed with the D_{2d} α-C orientation. The $Fe(S)_4$ core had T_d symmetry (S–Fe–S = 109.5°), and the Fe–S–C bond angle was 107.2°. The calculations describe a bonding pattern somewhat different from the above predictions (Figure 21 right). The Fe_σ-e($d_{xz,yz}$) orbitals are slightly higher in energy than the Fe_σ-b_2(d_{xy}) orbital, while the Fe_π-b_1($d_{x^2-y^2}$) and Fe_π-a_1(d_{z^2}) orbitals are split substantially with the Fe_π-b_1($d_{x^2-y^2}$) at higher energy. The calculated splitting pattern would be expected if the S_π interaction is large; however, based on the lack of significant S_π bonding in the model complex it appears the Xα–SW calculations overestimate this π interaction.

To date no spin-forbidden $^6A \rightarrow {}^4T$ d $\rightarrow$ d transitions have been observed in rubredoxin, therefore a comparison to the $^6A \rightarrow {}^4T$ transitions observed for $Fe(SR)_4^-$ is not possible. In contrast, a large amount of data exists on the spin-allowed charge-transfer transitions of *Cp* rubredoxin.[5,9,10,14,20] The single-crystal polarized charge-transfer absorption spectrum[60] for oxidized *Cp* rubredoxin as adapted from the work of Eaton and Lovenberg[14] is presented in Figure 20 (top) along with the polarized charge-transfer absorption for the model complex. *Cp* rubredoxin exhibits a weak ($\epsilon \approx 300$ M^{-1} cm^{-1}) charge-transfer band at $\sim$13 000 cm^{-1}. Based on the similarity in position and intensity to band A, this transition is assigned as the $S_\pi \rightarrow Fe_{\pi^*}$ transition. The lack of any significant MCD signal from this band in rubredoxin[14] rules out an assignment as a spin-forbidden transition, which will have a large C_0/D_0 ratio. The low intensity indicates that S_π bonding is also weak in rubredoxin. On the basis of group theory, there should be five electric dipole allowed $S_\sigma \rightarrow Fe_{\sigma^*}$ transitions (two *z* polarized and three *x,y* polarized). Two cleanly resolved *z*-polarized bands and at least two *x,y*-polarized bands are observed (Figure 20). From comparison with the model spectrum, the *z*-polarized transitions are assigned as the S_σ-$a_1 \rightarrow Fe_\sigma$-$b_2$($d_{xy}$) (29 000 cm^{-1}) and S_σ-e $\rightarrow Fe_\alpha$-e($d_{xz,yz}$) (17 600 cm^{-1}). An assignment of the *x,y*-polarized transitions is more difficult because only two of the three predicted bands are clearly observed. However, the CD spectrum of *Cp* rubredoxin[14] reveals the presence of an additional feature at 23 500 cm^{-1}, which cannot be correlated to any of the resolved absorption bands. The 23 500-cm^{-1} band is a strong candidate for the missing *x,y*-polarized absorption band. On the basis of a comparison to the model complex spectrum, the *x,y*-polarized bands are assigned as S_σ-$a_1 \rightarrow Fe_\sigma$-e($d_{xz,yz}$) (26 000 cm^{-1}), S_σ-$b_2 \rightarrow Fe_\sigma$-e($d_{xz,yz}$) (23 500 cm^{-1}), and S_σ-e $\rightarrow Fe_\sigma$-b_2(d_{xy}) (20 200 cm^{-1}). The most noticeable difference between the model and protein spectra is reversal of the energy order of the *z*- and *x,y*-polarized bands. This difference reflects the different energy splitting of the Fe d orbitals (Figure 21). From the splitting between the S_σ-$a_1 \rightarrow Fe_\sigma$-e($d_{xz,yz}$) and S_σ-$a_1 \rightarrow Fe_\sigma$-$b_2$($d_{xy}$) transitions, the Fe_σ-b_2(d_{xy}) orbital is estimated to be roughly 3000 cm^{-1} above the Fe_σ-e($d_{xz,yz}$) orbitals. The order of this splitting is as predicted from the S_σ bonding model for the D_{2d} geometry in Figure 21.

Qualitatively comparing the model spectrum to the protein spectrum reveals that the onset of the $S_\sigma \rightarrow Fe_\sigma$ charge-transfer manifolds occurs at about the same energy, indicating that the S_σ bonding levels in this region are similar in the two complexes. However, the S_σ-a_1 level in *Cp* rubredoxin is almost 4000 cm^{-1} lower in energy relative to the Fe_σ manifold than the S_σ-a level in the model complex. This difference between rubredoxin and the model complex most likely arises from the difference between the aryl and alkyl R group bonded to the sulfur.

The electronic structure of the rubredoxin active site (Figure 21) provides insight into its high rate of electron transfer. From the Mössbauer[17] data, reduced rubredoxin is known to have a d_{z^2} ground state, with the $d_{x^2-y^2}$ orbital at least 800 cm^{-1} higher in energy. While the orbital splitting pattern in oxidized rubredoxin is not experimentally known, our model studies predict the d_{z^2} orbital to also be the lowest Fe d orbital for the oxidized site. This indicates that the d_{z^2} orbital accepts the electron in the redox reaction of this active site. This orbital is almost nonbonding, and addition of an electron should have little effect on the site geometry. Thus the electronic structure in Figure 21 predicts that the electronic and nuclear reorganizational energy barrier will

(57) The dihedral angle is defined as the angle between the S–Fe–S plane, containing the S_4 molecular axis, and the Fe–S–α–C plane.

(58) Gewirth, A. A.; Solomon, E. I. *J. Am. Chem. Soc.* **1988**, *110*, 3811.

(59) On the basis of the anisotropic covalency model, *D* is expected to be negative in this geometry because $\beta^2 < \gamma^2$ (eq 24). This appears to be inconsistent with the observed ZFS for *Po* rubredoxin ($D = +1.68$ cm^{-1}; $E/D = 0.25$); however, for a system with a highly rhombic ZFS, it is very difficult to predict the sign of the ZFS. In addition, the crystal structure of *Po* rubredoxin has never been solved.

(60) The polarizations were calculated by assuming that the site has effective D_{2d} symmetry (geometry II) with the molecular *z* axis bisecting the S_6–Fe–S_{42} bond angle and the S_9–Fe–S_{39} bond angle.

(61) Butcher, K. B.; Gebhard, M. S.; Solomon, E. I., submitted for publication in *J. Am. Chem. Soc.*

be small for the rubredoxin active site. In addition, in the oxidized site the d_{z^2} and $d_{x^2-y^2}$ orbitals should be substantially split. If these orbitals were close to degenerate, reduction to give the ferrous ^5E ground state would result in a Jahn-Teller distortion; however, this splitting of these orbitals removes need for this distortion.

Acknowledgment. We thank the National Science Foundation [Grant CHE-8613376, (E.I.S.)] and the National Institutes of Health [Grants GM-36308 (M.M.) and GM-31849 (S.A.K.)] for support of this research. M.S.G. and J.C.D. acknowledge NSF for graduate research fellowships.

Variable Photon Energy Photoelectron Spectroscopy on $FeCl_4^-$: An Unusual Electronic Structure for High-Spin d^5 Complexes

Kristine D. Butcher,[†] Stephen V. Didziulis,[†] Bernard Briat,[‡] and Edward I. Solomon*,[†]

Contribution from the Department of Chemistry, Stanford University, Stanford, California 94305, and the Laboratoire d'Optique Physique, ESPCI, 10 rue Vauquelin, 75321 Paris 05, France.
Received August 28, 1989

Abstract: Variable energy photoelectron spectroscopy (PES) is used to elucidate the valence band electronic structure and bonding in tetrahedral d^5 $FeCl_4^-$. PES spectra obtained over the photon energy range 25-150 eV show intensity changes in the valence band features which indicate that more metal character is present in the deepest bonding levels. This is inverted from the normal electronic structure description of transition-metal complexes. The lack of off-resonance intensity in the deep binding energy satellite, which corresponds to a two-electron transition involving metal ionization plus ligand-to-metal charge transfer, indicates that little relaxation occurs on ionization. This result is confirmed by analysis of the satellite structure in the core level XPS Fe 2p spectra. PES spectra taken at the Fe 3p absorption edge, which provide insight into the bonding description of the ionized final state, show dramatic resonance intensity enhancement of the main band peaks as well as the satellite. The resonance enhancement of the main band indicates that it contains significant metal character after ionization and thus provides further evidence that the relaxation is small. A configuration interaction analysis shows that the resonance profiles of the photoelectron peak intensities at the absorption edge are also consistent with an inverted ground-state bonding scheme with little relaxation occurring upon ionization. Quantitative analysis of the resonance intensity data gives an experimental estimate of the covalent mixing in the HOMO as 38% Fe, 62% Cl. Both the inverted bonding scheme and the very small relaxation are reproduced by spin-unrestricted but not by the spin-restricted SCF-Xα-SW calculations. The origin of this unusual electronic structure in high-spin d^5 complexes and its implications with respect to redox chemistry are discussed.

I. Introduction

A significant effort has been directed toward understanding the electronic structure and bonding in high spin ferric complexes due to their presence in many protein active sites, particularly the iron-sulfur proteins such as rubredoxin.[1,2] The usual molecular orbital diagram for a metal complex places the metal 3d orbitals above the ligand, resulting in an antibonding HOMO which contains mostly metal character and bonding orbitals having mostly ligand contributions as shown in Scheme I. However, calculations for ferric-sulfur complexes have indicated that an unusual bonding description may be appropriate which, in fact, involves a HOMO containing mostly S 3p character.[1a] Our focus in these studies is on experimentally determining the actual bonding scheme present in a simple high-spin d^5 complex using PES. Toward this goal, we have extended our earlier studies on d^9 and d^{10} copper and zinc chlorides[3] to d^5 $FeCl_4^-$ to determine the electronic structure and its change upon ionization. These studies allow us to evaluate the relative roles of covalency and spin polarization in determining the ground-state bonding description. We must also evaluate the effects of final state relaxation on the PES spectrum as this can complicate interpretation of PES spectral results.

Our previous work on d^9 $CuCl_4^{2-}$ systems demonstrated that dramatic wave function changes occur upon ionization.[3a] This large final state relaxation results from a large change in metal-centered electron repulsion due to ionization. The orbitals relax in order to minimize the change in repulsion. As a result of this relaxation, intensity is shifted into deeper binding energy satellite peaks.[4] The satellite peak corresponds to the simultaneous ionization plus shakeup of a second electron to create an excited

Scheme I

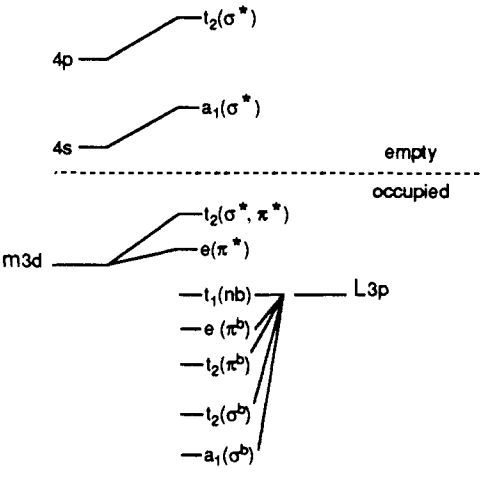

Scheme II

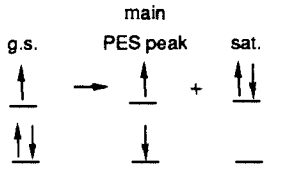

[†] Stanford University.
[‡] The Laboratoire d'Optique Physique.

0002-7863/90/1512-2231$02.50/0